ATLAS Internal Note
Muon-No-21
09 June 1993

Muon Rates in ATLAS

A. Cheplakov, A. Kriushin, V. Kukhtin, R. St.Denis

1 Introduction

This note describes the current understanding of particle rates in the muon chambers of ATLAS. The purpose is to take the previously calculated punchthrough and decay rates (see [1] and [2]) and compare them to rates from physics processes of interest. All of the work (except for the decay muons) has been done with the ISAJET Monte Carlo. All momenta are presented after being back–tracked to the origin. This is of particular interest for the punch–through and decay calculations.

There is quite a wealth of information in Volume II of the Aachen Workshop Report that should be considered together with these data. In particular, one must understand the theoretical problems associated with calculating the rates from heavy quark decays. Some of these problems are discussed below. The most important fact is that absolute rates could be in error by up to two orders of magnitude for muons having transverse momenta above 5 GeV/c, and even worse for those below 5 GeV/c. This tempers the conclusions that may be drawn, but we boldly go ahead nonetheless. Furthermore this error is expected to be reduced when better knowledge of gluon structure functions becomes available.

The muon rates have been calculated for the following sources:

- b quark decays;
- c quark decays;
- t quark decays ($m_{top} = 130$ GeV/c^2);
- W decays;
- Z decays;
- $\pi^{\pm}$,K_L, $K^{\pm}$ decays; (ISAJET plus punch-through probability distributions as described in much detail in [1] and [2])
- particles resulting from the punch through of hadrons (see [1] and [2]).

The note is organized as follows. First, descriptions of the physics issues involved in the generation of the various processes are discussed and important assumptions described. Next, the results are given for transverse momenta above 2 GeV/c for heavy quarks and down to lower momenta for other sources. Comparisons of these results to earlier results provide a check. Discussion of the effect of additional material in the calorimeter on these relative rates as well as a look at theoretical problems conclude this study.

2 Muon Rates From B Decays

All events were generated using ISAJET. The datacards are included below in the Appendix. Events were generated for all possible tree level parton scatterings; however, gluon scattering dominates by two orders of magnitude over other sources over the lower momenta ranges. Hence the higher order process of gluon splitting into b quarks dominates the production of these quarks over the tree-level rate (see fig. 1). This creates a technical difficulty in that one would have to generate many events which do not have a gluon splitting into b quarks. However, this is overcome by the following method.

In the event generation the parton cascade was carried out 10 times for each tree level scattering. The fragmentation was done only if there was a b quark in the cascade. Then this was also repeated 10 times for each b quark found. Finally, the event was analyzed each time the fragmented event contained at least one muon having transverse momentum above 2 GeV/c.

The parton transverse momenta were generated in separate groups with 10 or 20 GeV/c intervals. For partons having p_t between 10 GeV/c and 200 GeV/c, the intervals were 10 GeV/c. For p_t between 200 GeV/c to 620 GeV/c, the intervals were 20 GeV/c [1].

Four events were printed out in order to understand the implementation of the mechanism. The decay sequences in these events are shown below. Of these four events, all muons could be traced back to a primary b quark which had indeed come from a gluon splitting.

Further investigation of the origin of the muons was done by checking the ancestory of each muon back to its original quark. Table 1 shows the fractions of muons coming from various quarks for parton transverse momenta in three ranges: 50-60 GeV/c, 300-320 GeV/c, and 600-620 GeV/c. The muons had to have transverse momenta above 5 GeV/c. It can be seen that the effect of multiple quark splittings (where the second quark is a c quark) giving high momentum muons reaches at most 10% in the highest momentum bin.

The results for each of the plots were obtained by summing over all the jet energies, weighting by the cross section/event for each of the jet intervals. It is useful for those trying to compare results to look in the appendix for a description of the proper normalization one must use in ISAJET.

The intervals are given only to indicate the binsizes. All of these distributions are double differentials. For example, with the transverse momentum distribution, the cross sections are given in millibarns per unit muon rapidity per GeV/c of muon transverse momentum.

For the decay sequences in events examined by hand, the tree level parton generation

[1] This requires 40 jobs taking 10 hours each on a VAX 3100.

ΔP_t	50–60 GeV/c	300–320 GeV/c	600–620 GeV/c
N_μ	635	2317	2155
F_μ^u (%)	0.0	0.0	0.1
F_μ^d (%)	0.3	0.1	0.0
F_μ^s (%)	0.0	0.0	0.0
F_μ^c(%)	4.9	7.9	10.4
F_μ^b (%)	94.2	91.5	85.8
F_μ^t (%)	0.0	0.0	3.0
F_μ^g (%)	0.6	0.5	0.6

Table 1: Fraction of the time a muon came from a meson or baryon produced by each quark for variuos tree level transverse momenta. Top mass is 150 GeV.

was for partons having transverse momenta between 40 GeV/c and 50 GeV/c. Below, momenta (transverse momenta) are indicated for the b quarks and muons.

```
Event 1:
  22.1 GeV/c (22 GeV/c)
    b -- BD* -- BD ------ MU-     12.3 GeV/c (9 GeV/c)
             -- GA      -- ANUM
                        -- D+
  21.0 GeV/c (16 GeV/c)
 bbar -- DB  -- D-
             -- phi
             -- F*+ ----- F+ ------- MU+  1.5 GeV/c (1.3 GeV/c)
                      -- GA       -- NUM
                                  -- eta

Event 2:
  33.0 GeV/c (24 GeV/c)
    b -- BU* -- BU ------ D0* ------ D0  ----- MU+  7.5 GeV/c (5.3 GeV/c)
             -- GA      -- rho-     -- pi0     -- NUM
                        -- pi0                 -- K*-


Event 3:
  27.1 GeV/c (26 GeV/c)
    b -- BU* -- BU ------ D0
             -- GA      -- MU- 10 GeV/c (7.9 GeV/c)
                        -- omega

  31.6 GeV/c (22 GeV/c)
```

```
 bbar -- DB* -- DB ------ tau+ ---- MU+ 3.1 GeV/c (3.0 GeV/c)
             -- GA      -- NUT     -- NUM
                       -- D-      -- ANUT

Event 4:
  33.7 GeV/c (30.7 GeV/c)
 bbar -- UB* -- UB --- MU+ 5.6 GeV/c (5.1 GeV/c)
             -- GA  -- D0Bar* --  D0bar -- MU- 9.5 GeV/c (8.8 GeV/c)
                    -- D0      --  GA    -- ANUM
                                       -- K*+
```

3 Muon Rates From C Decays

The methods for generating C quarks are the same as for the B quarks. Events were also checked by hand to see that things made sense.

4 Muon Rates from W and Z Decays

The generation of these events is reasonably straightforward. Again, a number of jobs must be run for various intervals of IVB transverse momenta. One need only consider whether muons prefer to get their transverse momenta from recoil of the IVB against a gluon or by having the IVB off its mass shell. This is important because in the limit of large momentum, the cross sections both go like $1/p_t^4$ and so the ratio of the strong and weak forces determines the sharing of how far each must be off its mass shell. However the resonance is rather dominant for the transverse momenta we considered here. The ranges of values that are considered for the virtual IVB masses are listed in the appendix.

5 π,K^0, K^+, K^- decays and Punch through of pions from jets

Punch through rates for pions have been studied in detail in muon notes [1] and [2]. However it is worth recalling that the minimum bias cross sections lead to the largest overall uncertainty, a factor of 5, in total rates in the muon system. If one considers only the muons from punchthrough or the hadrons from punchthrough, then there is probably an additional factor of between 10 and 50 uncertainty due to inadequate parameterization of the momentum spectrum of the punchthrough particles and discrepancy with or lack of comparison with experimental data.

An important feature of the comparison of these rates to the other physics process is the need to back-track the momentum of the particles as they exit the calorimeter to the original momentum at the vertex. Since the particles are distributed uniformly in rapidity, it is safe to average the energy loss over the interval of rapidity considered in the momentum spectra. This averaging procedure is described in the next section.

6 Energy Loss Thresholds

If one considers a simple model of a detector as a cylindrical block of iron with a hole removed to create a central cavity, then the back-tracked momentum, p', and transverse momentum, p'_t, can be calculated as a function of the measured momentum p and transverse momentum, p_t (see Appendix and fig 2 for details):

$$(1) \qquad p_t'^{barrel} = p_t + \Delta L_{barrel} \frac{dE}{dl},$$

$$(2) \qquad p'^{barrel} = p + \frac{1}{\sin\theta} \Delta L_{barrel} \frac{dE}{dl},$$

$$(3) \qquad p_t'^{endcap} = p_t + \frac{-1}{\sinh\eta} \Delta L_{endcap} \frac{dE}{dl},$$

$$(4) \qquad p'^{endcap} = p + \frac{1}{\cos\theta} \Delta L_{endcap} \frac{dE}{dl},$$

where ΔL_{barrel} (ΔL_{endcap}) is the number of radiation lengths in the barrel (endcap), dE/dl is the energy loss per interaction length, and the primed variables are those derived from the measured values. Recall that $\eta = \log(\cot(\theta/2))$, and theta is the polar angle where the z axis is along the beam direction.

Note that the equations for momentum are very intuitively appealing in the sense that they imply that the momentum at the vertex is always larger than that observed by an amount that is at least equal to what one expects from the simple energy loss. In the barrel, the momentum loss grows rapidly with pseudorapidity while in the endcap it is a much slower function. On the other hand, the case for transverse momentum is much less intuitive. First of all, in the barrel, even though the material gets thicker as pseudorapidity increases, the shift in transverse momentum remains constant. What seems even stranger is that in the endcap the shift in transverse momentum is always less than the simple endcap thickness times momentum loss per unit length formula. This is of course taken care of in the equations by noting that the momentum is getting much larger for a fixed transverse momentum and increasing pseudorapidity. Referring to the figure, one sees that instead of getting a 14×0.22 GeV/c = 3.08 GeV/c shift at $\eta = 3$, one gets only about a 0.3 GeV/c – the factor of 10 ratio of p to p_t. Hence one needs to add ten times more material in the endcap to get an equivalent reduction in rate in the barrel.

Since the distribution of the source particles is flat in pseudorapidity, integrating over some portion of pseudorapidity (as is shown in the figures) will shift the momentum spectrum by the average of $\Delta p \equiv p' - p$ (or $\Delta p_t \equiv p'_t - p_t$). The functions, $\Delta p(\eta)$ and $\Delta p_t(\eta)$ are shown in Fig 40. The geometry used (fig. 2) for calculations of the punchthrough rates was somewhat more complicated in that the inner cavity made the transition from barrel to endcap at a different angle ($\theta = 22.9$ degrees, $\eta = 1.60$) than the outer part of the calorimeter ($\theta = 35.9$ degrees, $\eta = 1.13$). Therefore, the above functions are shown twice. Once one assumes the transition is that of the inner cavity, and in the other case, the transition point is taken as that of the outer cavity. This affects the average shift in the region where the transition actually occurs ($1.0 \leq \eta \leq 2.0$). Fig 40 also indicates the average of these functions over the three regions of pseudorapidity as

well as over the entire pseudorapidity coverage of the muon system. The values of these averages are shown in Table 6. The analytical formulas for the average $\Delta p(\eta)$ and $\Delta p_t(\eta)$ are:

$$\Delta p_t(\eta)^{barrel} = \frac{1}{\eta_2 - \eta_1} \Delta L_{barrel} \frac{dE}{dl}, \tag{5}$$

$$\Delta p(\eta)^{barrel} = \frac{1}{\eta_2 - \eta_1} \Delta L_{barrel} \frac{dE}{dl} \left(\cot\theta_2 - \cot\theta_1\right), \tag{6}$$

$$\Delta p(\eta)^{endcap} = \frac{1}{\eta_2 - \eta_1} \Delta L_{endcap} \frac{dE}{dl} \left(\log \frac{\tanh\eta_2}{\tanh\eta_1}\right), \tag{7}$$

$$\Delta p(\eta)^{endcap} = \frac{1}{\eta_2 - \eta_1} \Delta L_{endcap} \frac{dE}{dl} \left(\log \frac{\tan\theta_1}{\tan\theta_2}\right). \tag{8}$$

For the calculation of the spectrum of particles from punchthrough and decay, the largest shifts for $1.0 \leq |\eta| \leq 2.0$ were used, meaning the geometry corresponding to the inner configuration was used.

Inner				
	$\|\eta\| \leq 1.0$	$1.0 \leq \|\eta\| \leq 2.0$	$2.0 \leq \|\eta\| \leq 3.0$	$\|\eta\| \leq 3.0$
Δp_t (GeV/c)	2.64	2.00	0.53	1.72
$\Delta p(GeV/c)$	3.10	4.46	3.13	3.56
Outer				
	$\|\eta\| \leq 1.0$	$1.0 \leq \|\eta\| \leq 2.0$	$2.0 \leq \|\eta\| \leq 3.0$	$\|\eta\| \leq 3.0$
Δp_t (GeV/c)	2.64	1.57	0.53	1.58
$\Delta p(GeV/c)$	3.10	3.52	3.13	3.25

Table 2: Average energy shift for various intervals for pseudorapidity. Inner and Outer differ in the polar angle at which the barrel and endcap meet.

7 Check of Integrated Rates Against Previous calculations

A check of the rates calculated here was made by comparing the following integral rates ($|\eta| \leq 3.0$):

- the sum of the b and c quark integral rates (Fig. 3);
- top ($m_{top} = 130$ GeV/c^2) (Fig. 4);
- decays and punchthrough (Fig. 5);
- W decays (Fig. 6);
- Z decays (Fig. 7);

In all cases there is satisfactory agreement. Furthermore, in all of these comparisons, the results are shown without any muon momentum cutoff that would arise from the absorption of low momentum muons in the calorimeter material.

8 Cross Sections

The results for the various contributions to the cross section are given in Figs. 8 through 39. Figs. 8 to 15 show the differential cross sections for integrals over $|\eta| \leq 1.0$, $1.0 \leq |\eta| \leq 2.0$, $2.0 \leq |\eta| \leq 3.0$, and $|\eta| \leq 3.0$ and plotted as a function of the transverse momentum on maximum scales of 600 GeV/c and 50 GeV/c. Observe that there is a sharp cutoff in the transverse momentum at the value corresponding to those muons that would be absorbed by the calorimeter. This cutoff would of course not be as sharp as shown because of acceptance; such effects have not been considered here.

One sees that the the b and c quark contributions dominate down to transverse momenta of about 5 GeV/c where the decay contributions rise rapidly and overcome the heavy quark rates. The corresponding integral cross sections are shown in figs. 16 to 23. The entire exercise is repeated in terms of momentum in figs. 24 to 31 for differential cross sections and figs. 32 to 39 for integral cross sections.

It is interesting to consider the effect of additional material on the relative rates of sources of particles in the muon chambers. The curves of course remain in the same place; however, the minimum momentum possible is increased. This decreases the total cross section. The amount of this increase per unit lambda depends on whether one is interested in p or p_t and the rapidity. As discussed above, the physics is best described in p_t but the filtering or decreasing of rate is in p. This leads to the unfortunate situation described by the curves in fig. 40. The average effect on barrel rates is to change the p_t threshold by 2.64 GeV in 12 interaction lengths or 0.22 GeV/c/λ. For the endcaps, the effect is much smaller, changing by only 0.53 GeV/c in 14 interaction lengths or 0.038 GeV/c/λ. For a p_t spectrum falling as the eighth power, this corresponds to a rate decrease of 6%/λ, or something like 6 Hz/cm^2/λ out of a 100 Hz/cm^2 rate on the endcap.

9 Calculation of the Low Momentum Muons

In these calculations, values as low as 3 GeV/c in momentum – that is a transverse momentum of 300 MeV/c at η =3, have been used. In fact, for the above plots we have gone only to 2 GeV/c in transverse momentum for b and c quarks. It is worth giving some thought to the reliability of these calcuations. There are the following problems:

- Calculating the splitting function for gluons to heavy quarks at low momentum;
- Calculating the cross section for the tree level scattering;
- Lack of knowledge of the gluon structure function itself;
- Calculating the mass threshold behaviour of the b and c quarks.

This problem concerning the gluon structure function exists for all values of transverse momentum. The problems of gluon splitting and tree level cross sections become worse for low momentum muons. Finally, the problem of threshold behaviour is in fact not so poorly understood [3]. In considering the validity of the calculation, one must be careful about the Q^2 values which were being considered. For this dicussion, Q^2 will be taken as p_t^2. The hard scattering must have reasonable $p_t \equiv p_t^{tree}$ and the gluon that was split must have reasonable $p_t \equiv p_t^{heavy}$. Therefore, one must be careful that muons are coming from p_t^{heavy} and p_t^{tree} that are at least 10 - 15 GeV/c. If either of both p_t^{heavy} and p_t^{tree} go below this limit, then one is really entering the realm of minimum bias physics. This implies therefore that one should also be looking at the predictions for muon rates from minimum bias generators and trying to tie these to the usual jet generators at low transverse momentum. Additionally, as p_t^{heavy} approches p_t^{tree}, the time scales for these processes are similar and it is difficult to factorize the splitting from the hard scattering in this calculation. That is, the leading log approach breaks down.

9.1 Method for estimate

An estimate is however needed. Therefore, the program is just run down to its lowest possible parton cutoff of 2 GeV/c in transverse momentum. Note that if one says that a muon carries roughly 10% of this tree level parton transverse momentum and then adds in the factor of 10 to get to η =3, then one can at least technically generate down to 2 GeV/c momentum. One can look at the figures for the b and c quarks and see that in fact the behaviour is understandable. As one decreases the transverse momentum, the strong coupling runs, becoming larger. The effect of this running of the strong coupling is to make the apparent exponent in the p_t^{-n} to go from the point-like value of about 4 to large values, like 6 [2]. As the transverse momentum decreases, the effects of the b and c quark masses begin to suppress the cross section. In fact, by comparing the curves for b and c quarks, one can see that the b quark momentum curve turns over as one goes to low transverse momentum, doing so sooner than the c quark because the b quark has a heavier mass.

10 Conclusions

The cross sections for various sources of particles in the ATLAS muon system have been calculated for various regions of interest and compared to previous calculations. The dominant rates come from decays of hadrons in flight before they reach the calorimeter and for transverse momenta below 5 GeV/c. Above this value, the dominant rate comes from b quark decays. The uncertainties in the cross section for decays in flight are about a factor of five and those for the b and c decays are considerably larger. More reliable estimates will be possible when there are new results on the low x behaviour of structure functions, particularly when information on the gluon structure function become available. The reduction of absolute rate is quite ineffective because the filtering is needed in transverse momentum while the material filters in momentum. Where the rates are

[2] Recall this number was more like n=8 for the ISR.

high, on the endcap, p_t filtering is most ineffective. Furthermore, there is nothing to be done about the muon decay rate "wall" since additional material filters the muons from the interesting physics processes as well as those from decays.

References

[1] A.Cheplakov et al., ASCOT/EAGLE Internal Note MUON-NO-006, 1992

[2] A.Cheplakov et al., ASCOT/EAGLE Internal Note MUON-NO-013, 1992

[3] Private communication with T. Sjörstrand.

Acknowledgements

We would like to thank Leandro Nisati for help in using the correct cards and methods for ISAJET in the muon generation. We would also like to thank T. Sjörstrand for useful discussions about minimum bias event generation, heavy quark calculations and theoretical uncertainties.

11 Appendices

This section gives some technical details concerning the results obtained.

11.1 ISAJET datacards used for b and c quarks

```
MBL035
16000.,1000,1,200/
TWOJET
JETTYPE1
'ALL'/
JETTYPE2
'ALL'/
NEVOLVE
10/
NHADRON
10/
PT
500.,520.,500.,520./
SEED
2634670935/
```

```
HMASS
300./
TMASS
150.,-1.,-1./
WMASS
80.5,91.16/
END
STOP
```

11.2 ISAJET datacards used for W and Z generation

A sample set of data cards is given as follows:

```
MWL001
16000.,1000,1,200/
DRELLYAN
JETTYPE1
'MU+','MU-'/
JETTYPE2
'MU+','MU-'/
QTW
10.,20./
QMW
30.,70./
WTYPE
'W+','W-'/
SEED
2234670901/
HMASS
300./
TMASS
150.,-1.,-1./
WMASS
80.5,91.16/
END
STOP
```

QTW specifies the W or Z transverse momentum and QMW specifies the range of virtual W or Z masses.Note that for Z's, the WTYPE card is just Z. Values of QMW were 1. - 30., 30. - 70., 70. - 100., 100. - 200., 200. - 500., 500. - 1000.

11.3 Normalization in b and c quark generation

Using the proper normalization for the histograms of muon momenta in the b and c quark generation is somewhat delicate. The ISAJET output looks like the following:

$$
\begin{aligned}
&(9) && MONTE\ CARLO\ JET\ CROSS\ SECTION &&= 0.1852E-01MB\\
&(10) && EQUIVALENT\ INTEGRAL\ LUMINOSITY &&= 0.5400E+07/MB\\
&(11) && NUMBER\ OF\ ACCEPTED\ EVENTS &&= 1433\\
&(12) && FRACTION\ OF\ ACCEPTED\ EVENTS &&= 0.1431E-01\\
&(13) && CROSS\ SECTION\ FOR\ ACCEPTED\ EVENTS &&= 0.2649E-03
\end{aligned}
$$

Since ISAJET uses the same tree level scattering for ten evolutions and ten fragmentations, when one calculates the total cross section exposure for a run, one must take each of the tree level cross sections and multiply by 100. Since 1000 such tree level scatterings were requested, the effective number of events is 100000. It is clear that if one is often in a position where the same tree level diagram is used more than once (creating b quarks and muons more often than one time in 100), statistical correlations will be introduced and interpretation of the final results will be difficult.

In the above equations, one can check what has been done. First, the MONTE CARLO JET CROSS SECTION is in fact the sum of all tree level scatterings for the 100000 effective events. This can be checked against the CROSS SECTION FOR ACCEPTED EVENTS which represents the total tree level cross section for events passing the quark heavy flavor and muon criteria and the exact fraction of times that these tree level events were used. Observe that dividing the MONTE CARLO JET CROSS SECTION by 100000 or the CROSS SECTION FOR ACCEPTED EVENTS by 1433 gives about the same value for the cross section per event (0.1852E-06). Also observe that the ratio of the NUMBER OF ACCEPTED EVENTS to the FRACTION OF ACCEPTED EVENTS is about 100000. The weighting for each histogram bin started with

CROSS SECTION FOR ACCEPTED EVENTS/NUMBER OF ACCEPTED EVENTS

and then included factors for the two binwidths in the double differential (p_t and η).

11.4 Calculation of the Energy Losses for Backtracking

If one considers a barrel geometry, then for some polar angle, the material crossed by an infinite momentum track is $l = \Delta L_{barrel}/\sin\theta$ (see fig 2). Therefore, one easily sees that the momentum at the vertex is:

$$
\begin{aligned}
&(14) && p^{barrel} &&= p + \Delta p\\
&(15) && &&= p + l\frac{dE}{dl}\\
&(16) && &&= p + \frac{1}{\sin\theta}\Delta L_{barrel}\frac{dE}{dl},
\end{aligned}
$$

and, since $p_t = p\sin\theta$,

$$p_t'^{barrel} = p'\sin\theta \tag{17}$$
$$= (p+\Delta p)\sin\theta \tag{18}$$
$$= p_t + \Delta p\sin\theta \tag{19}$$
$$= p_t + l\frac{dE}{dl}\sin\theta \tag{20}$$
$$= p_t + \frac{1}{\sin\theta}\Delta L_{barrel}\frac{dE}{dl}\sin\theta \tag{21}$$
$$= p_t + \Delta L_{barrel}\frac{dE}{dl}, \tag{22}$$

In the endcap, the material traversed by the same track is $l = \Delta L_{endcap}/\cos\theta$ so that the previous equations become (for the endcap):

$$p'^{endcap} = p + \Delta p \tag{23}$$
$$= p + l\frac{dE}{dl} \tag{24}$$
$$= p + \frac{1}{\cos\theta}\Delta L_{endcap}\frac{dE}{dl}, \tag{25}$$

and, since $p_t = p\sin\theta$,

$$p_t'^{endcap} = p'\sin\theta \tag{26}$$
$$= (p+\Delta p)\sin\theta \tag{27}$$
$$= p_t + \Delta p\sin\theta \tag{28}$$
$$= p_t + l\frac{dE}{dl}\sin\theta \tag{29}$$
$$= p_t + \frac{1}{\cos\theta}\Delta L_{endcap}\frac{dE}{dl}\sin\theta \tag{30}$$
$$= p_t + \tan\theta\Delta L_{endcap}\frac{dE}{dl}. \tag{31}$$

Since $\eta = \log(\cot(\theta/2))$, $\cot(\theta/2) = \exp(\eta)$ and $\tan(\theta/2) = \exp(-\eta)$. Therefore, using the double angle formula for $\tan\theta$,

$$\tan\theta = \frac{2\tan(\theta/2)}{1-\tan^2(\theta/2)} \tag{32}$$
$$= \frac{2}{\cot(\theta/2)-\tan(\theta/2)} \tag{33}$$
$$= \frac{2}{\exp(\eta)-\exp(-\eta)} \tag{34}$$
$$= \frac{1}{\sinh\eta}, \tag{35}$$

it is possible to write

$$p_t' = p_t + \frac{1}{\sinh \eta} \Delta L_{endcap} \frac{dE}{dl}. \tag{36}$$

In order to obtain the average shift in momentum over some interval of η, one has to integrate the above equations over this range and divide by the difference in the two pseudorapidity values. This requires that we integrate $1/\sin\theta$,$1/\cos\theta$, and $1/\sinh\eta$ over $d\eta = d\theta/\sin\theta$:

$$\int \frac{d\eta}{\sin\theta} = \int \frac{d\theta}{\sin^2\theta} \tag{37}$$

$$= -\cot\theta, \tag{38}$$

$$\int \frac{d\eta}{\cos\theta} = \int \frac{d\theta}{\sin\theta\cos\theta} \tag{39}$$

$$= \int \frac{d(2\theta)}{2\sin\theta\cos\theta} \tag{40}$$

$$= \int \frac{d(2\theta)}{\sin 2\theta} \tag{41}$$

$$= \log(\cot\theta). \tag{42}$$

Given these integrals, one arrives at the final equations in the text.

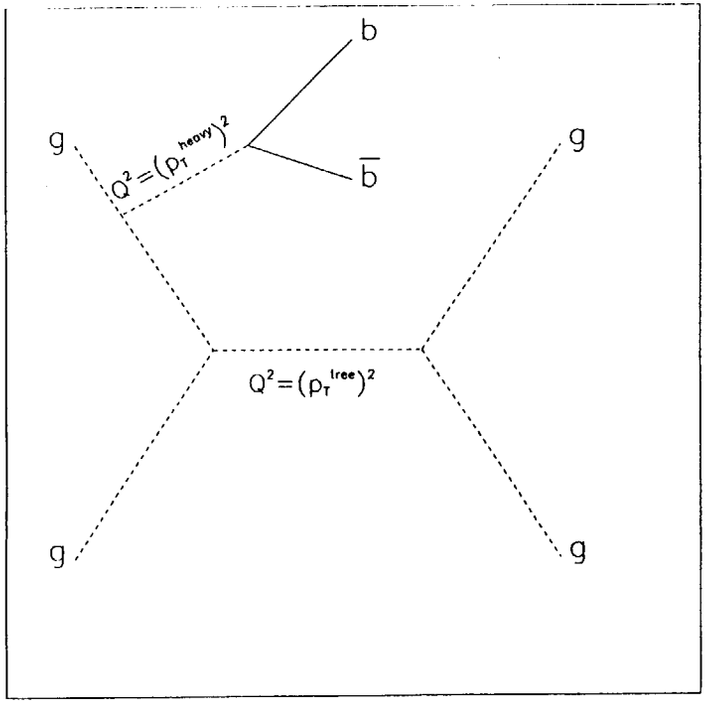

Figure 1: The dominant process for the production of b and c quarks is depicted here. The dashed lines represent gluons which are fusing at tree level. A bremstrahlung gluon splits to produce the heavy flavors. This can of course occur in the final state as well.

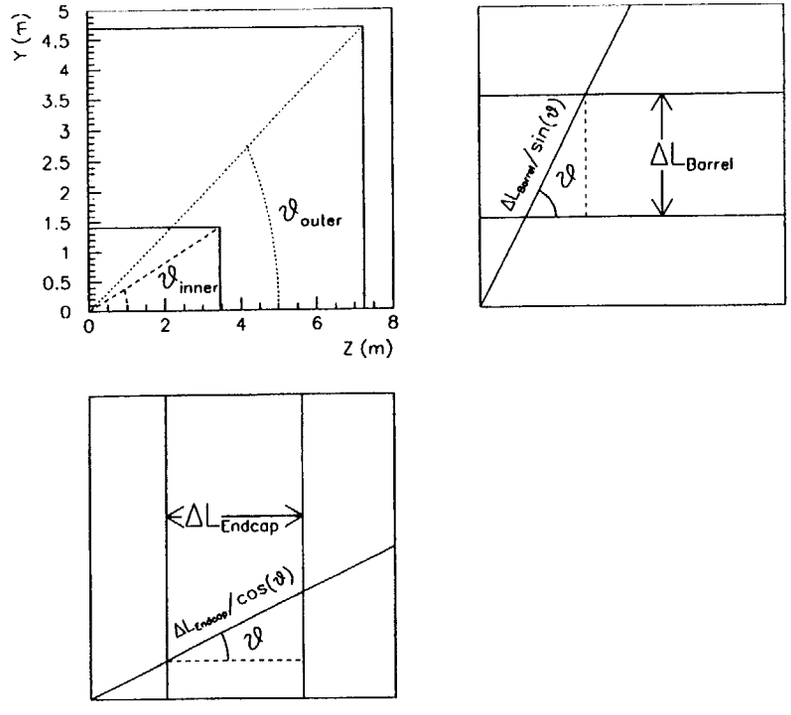

Figure 2: Geometry used for calculation of the backtracking of the muon momenta as measured in the muon chambers to that at the vertex. The three figures show the geometry of the inner cavity and the outer shell as well as the material seen by a track passing through barrel and endcap regions.

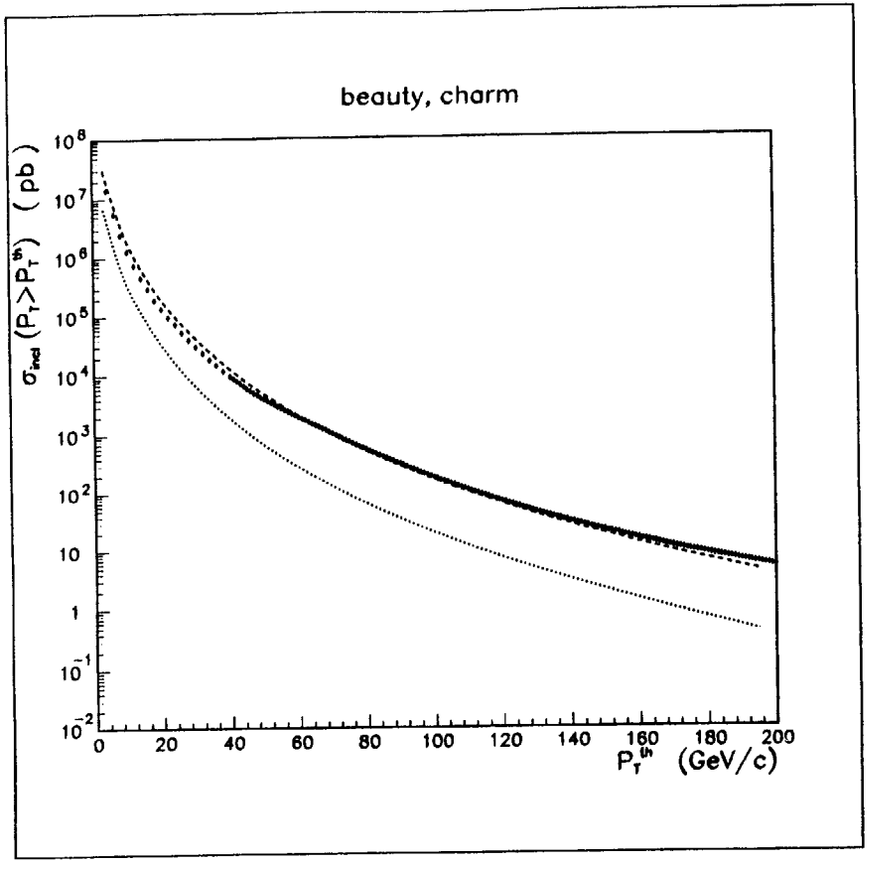

Figure 3: Comparison of b (dashed) and c (dots) quark integral cross sections ($|\eta| \leq 3$) with earlier results (diamonds).

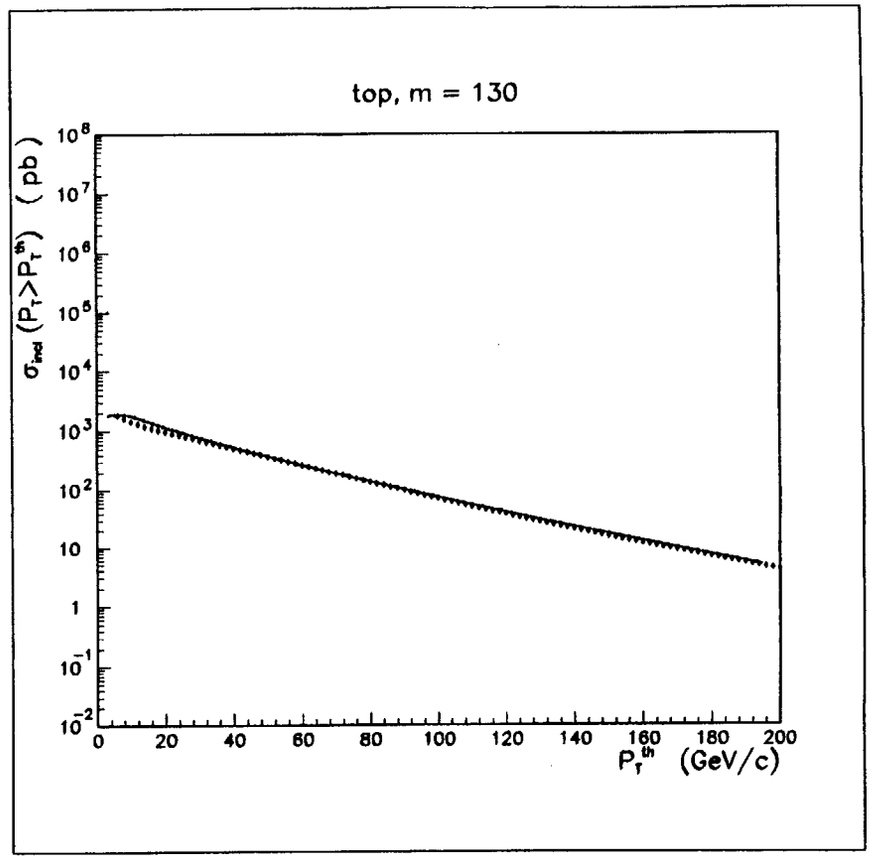

Figure 4: Comparison of top quark integral cross sections ($|\eta| \leq 3$, m_{top} = 130 GeV/c^2, dot-dash) with earlier results (diamonds).

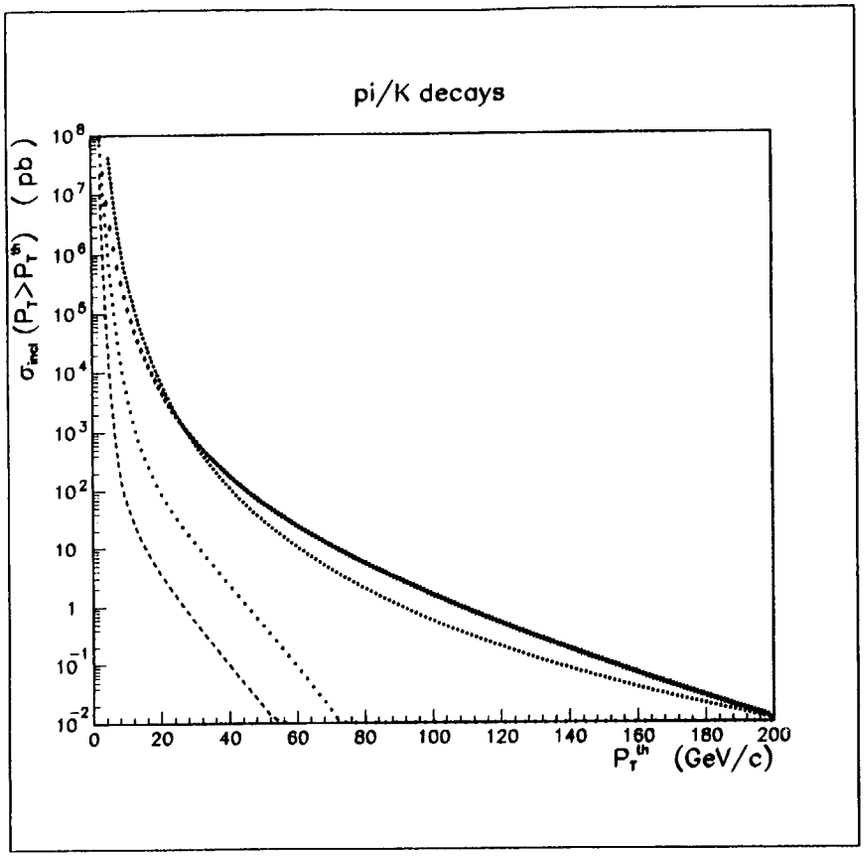

Figure 5: Comparison of decay integral cross sections (dots) ($|\eta| \leq 3$) with earlier results (diamonds). The muons from punchthrough (dots) and hadrons from punchthrough (dashes) are also shown.

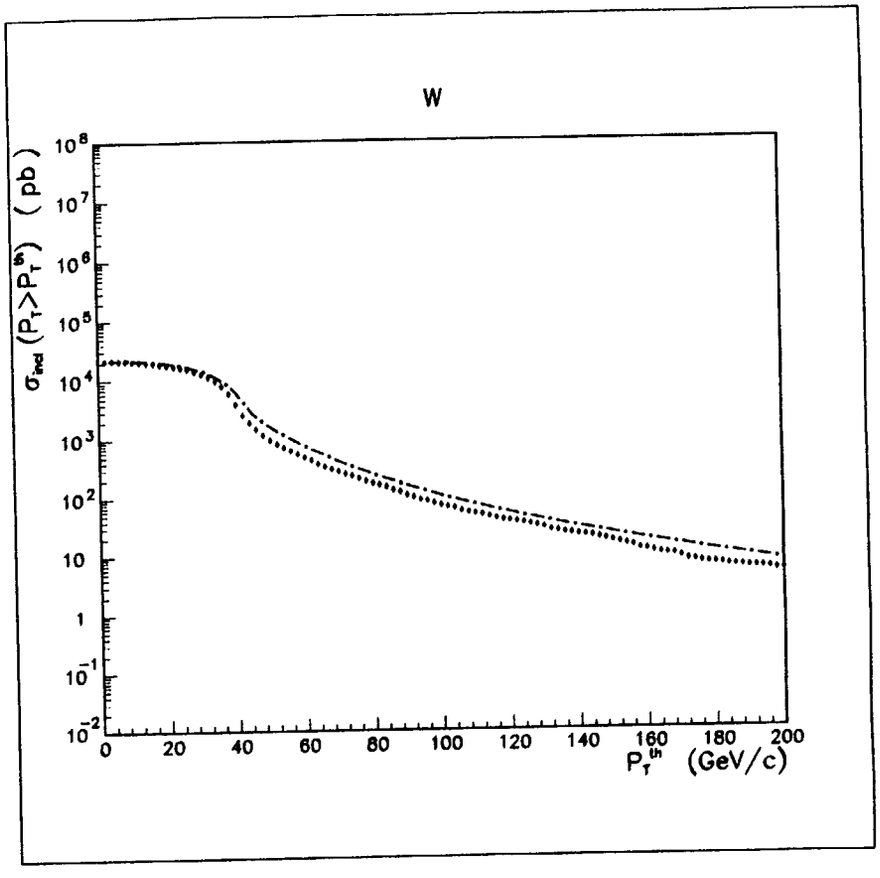

Figure 6: Comparison of W integral cross sections ($|\eta| \leq 3$, dot-dash) with earlier results (diamonds).

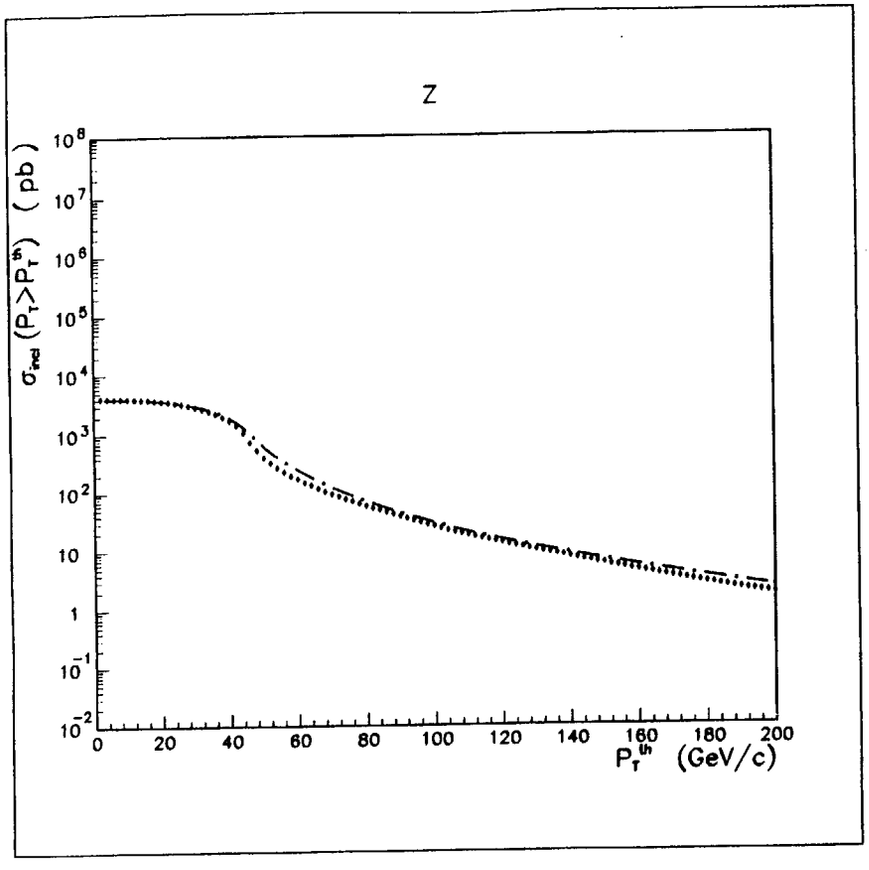

Figure 7: Comparison of Z integral cross sections ($|\eta| \leq 3$, dot–dash) with earlier results (diamonds).

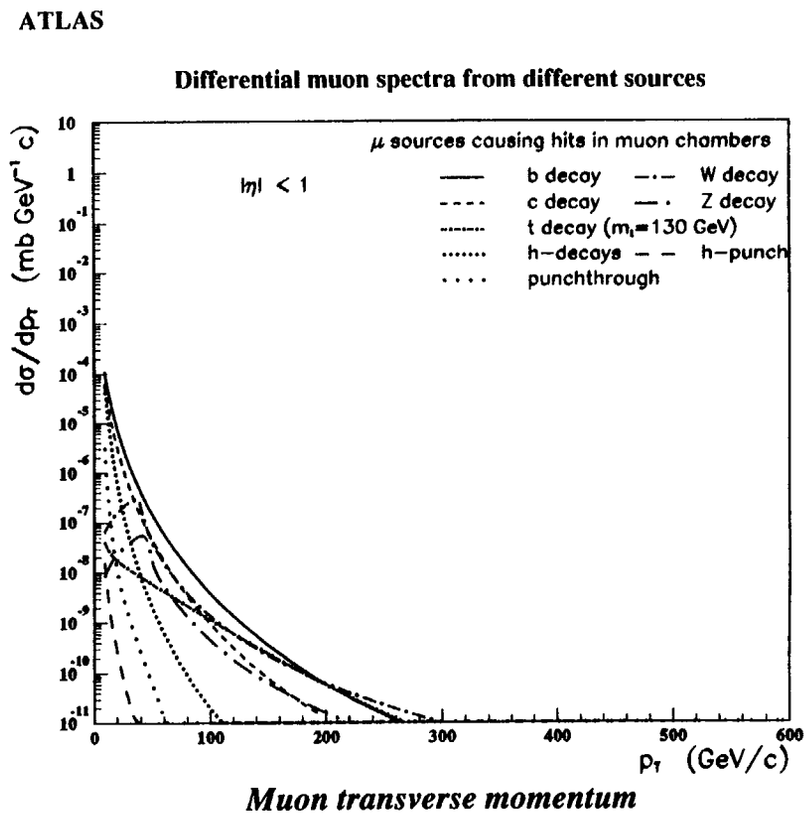

Figure 8: Differential cross sections of various sources of particles in the ATLAS muon system shown as a function of transverse momentum for $|\eta| \leq 1.0$.

ATLAS

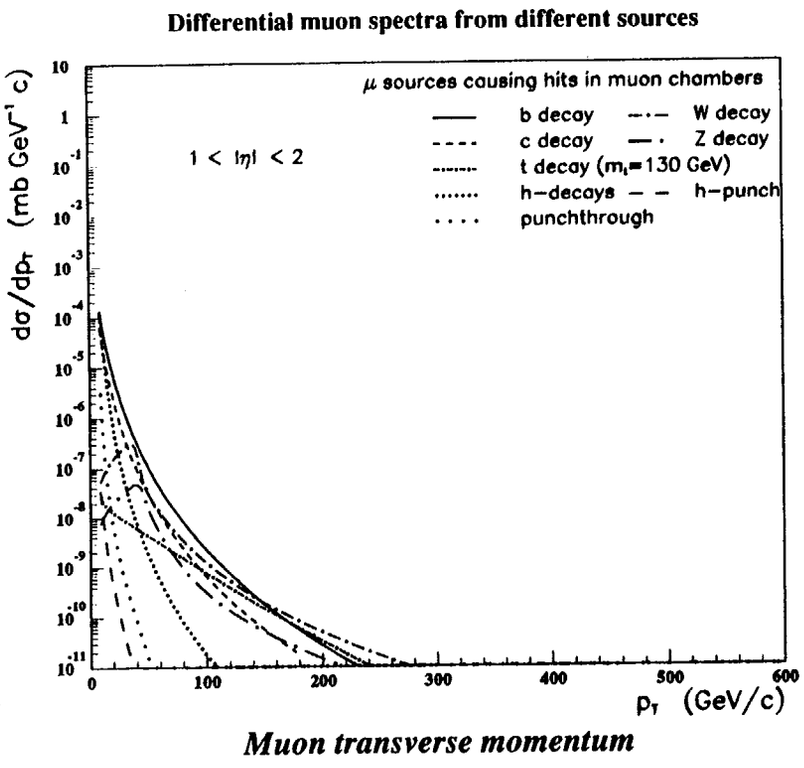

Figure 9: Differential cross sections of various sources of particles in the ATLAS muon system shown as a function of transverse momentum for $1.0 \leq |\eta| \leq 2.0$.

ATLAS

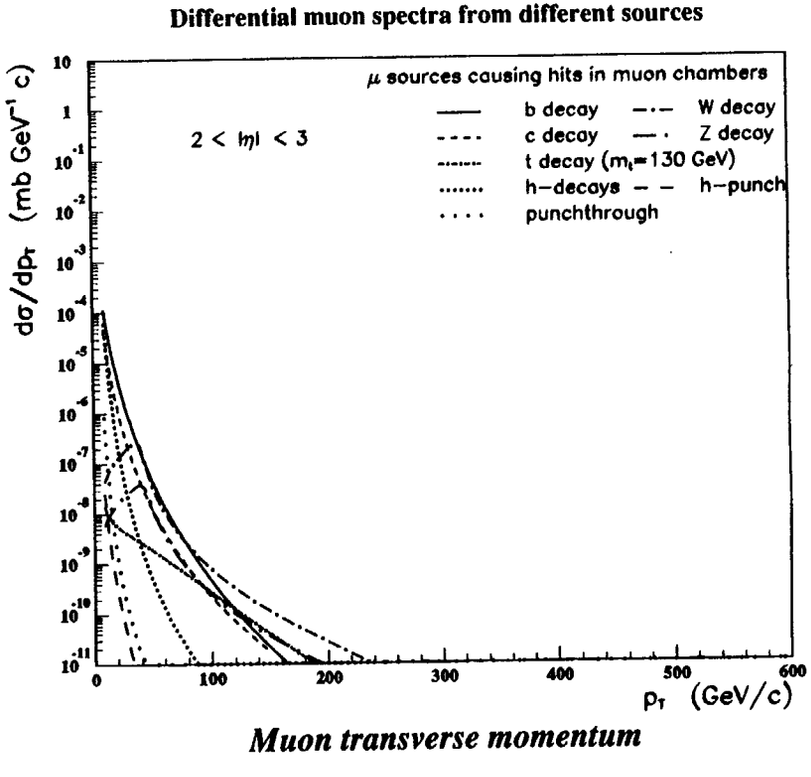

Figure 10: Differential cross sections of various sources of particles in the ATLAS muon system shown as a function of transverse momentum for $2.0 \leq |\eta| \leq 3.0$.

ATLAS

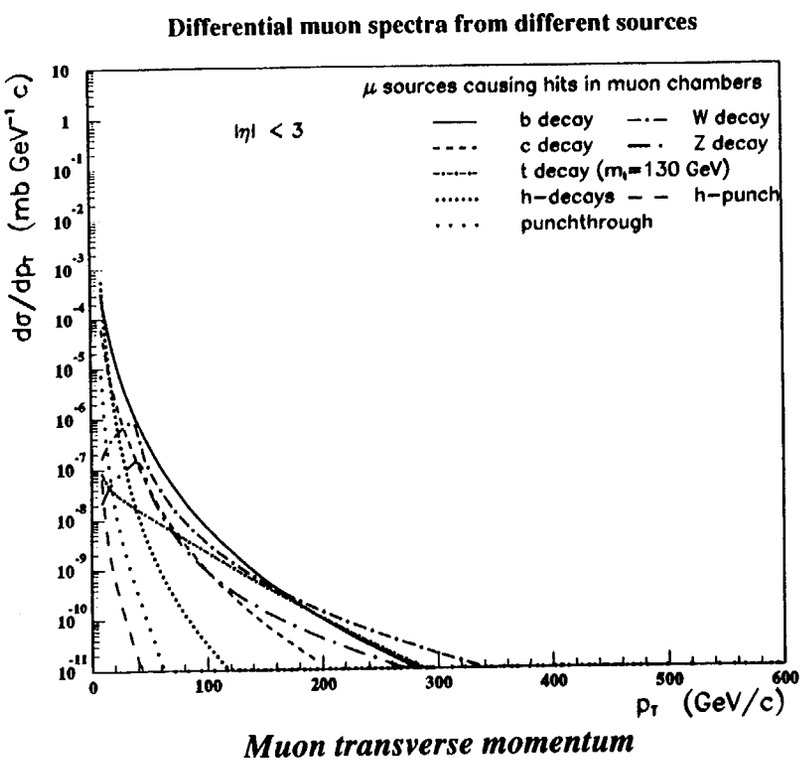

Figure 11: Differential cross sections of various sources of particles in the ATLAS muon system shown as a function of transverse momentum for $|\eta| \leq 3.0$.

ATLAS

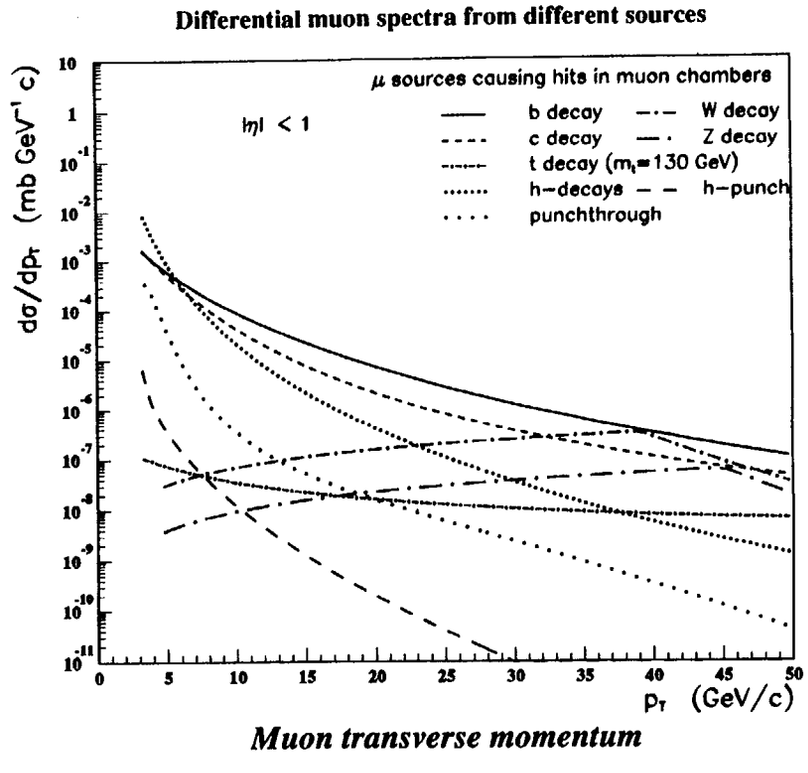

Figure 12: Differential cross sections of various sources of particles in the ATLAS muon system shown as a function of transverse momentum for $|\eta| \leq 1.0$.

ATLAS

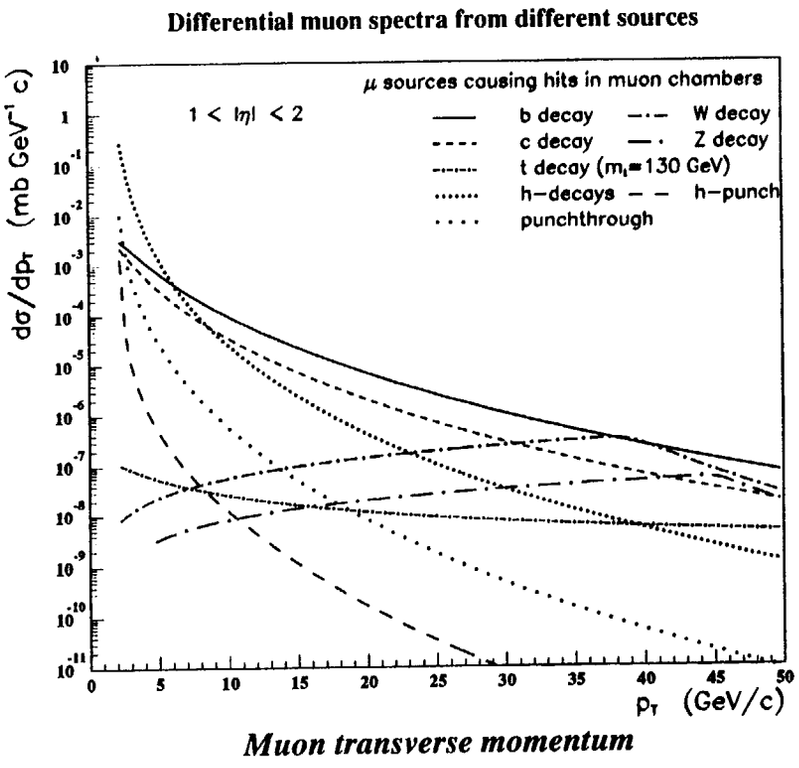

Figure 13: Differential cross sections of various sources of particles in the ATLAS muon system shown as a function of transverse momentum for $1.0 \leq |\eta| \leq 2.0$.

ATLAS

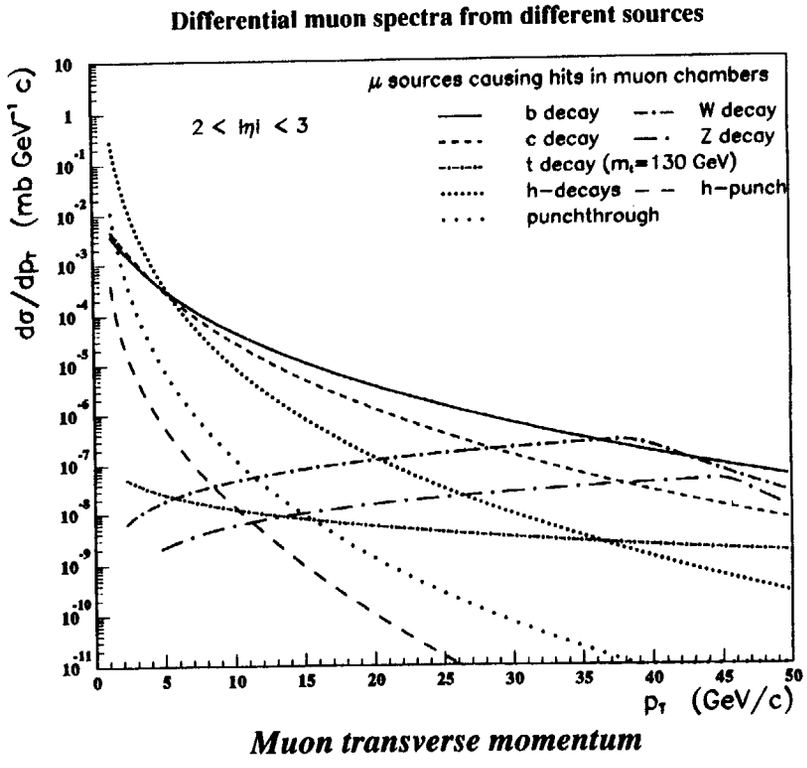

Figure 14: Differential cross sections of various sources of particles in the ATLAS muon system shown as a function of transverse momentum for $2.0 \leq |\eta| \leq 3.0$.

ATLAS

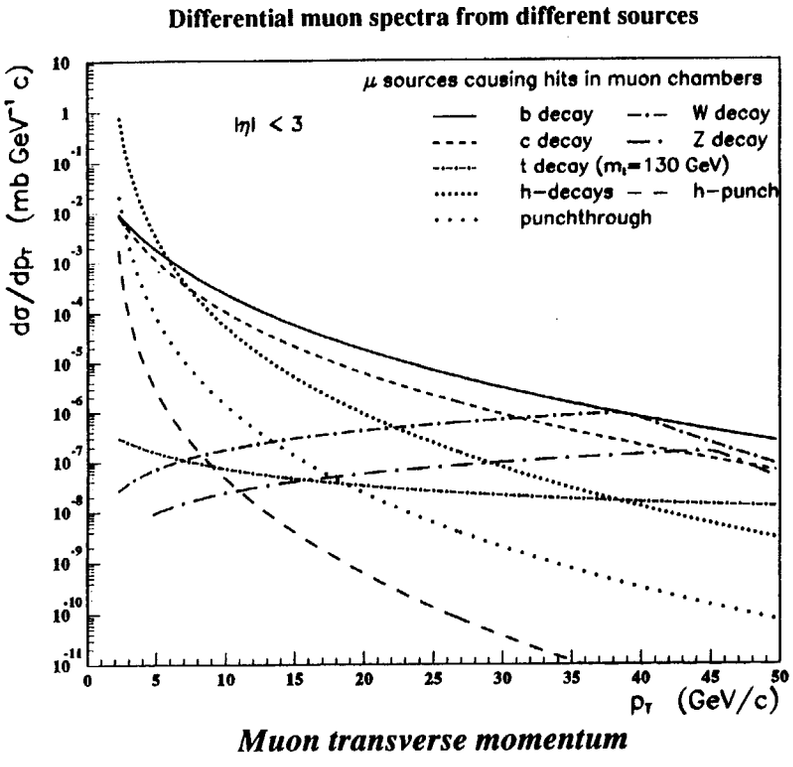

Figure 15: Differential cross sections of various sources of particles in the ATLAS muon system shown as a function of transverse momentum for $|\eta| \leq 3.0$.

ATLAS

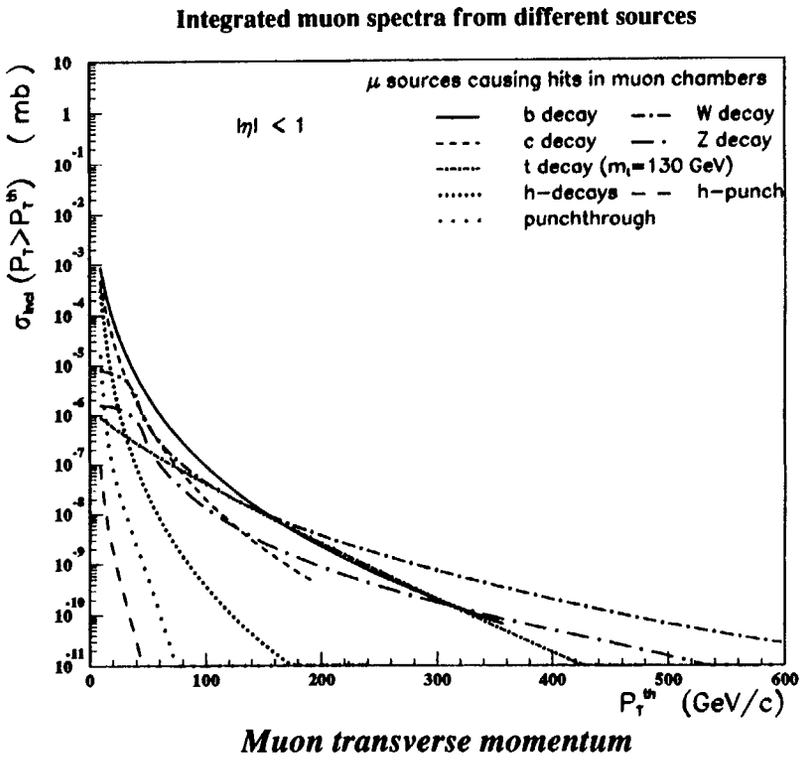

Figure 16: Integral cross sections of various sources of particles in the ATLAS muon system shown as a function of the transverse momentum threshold for $|\eta| \leq 1.0$.

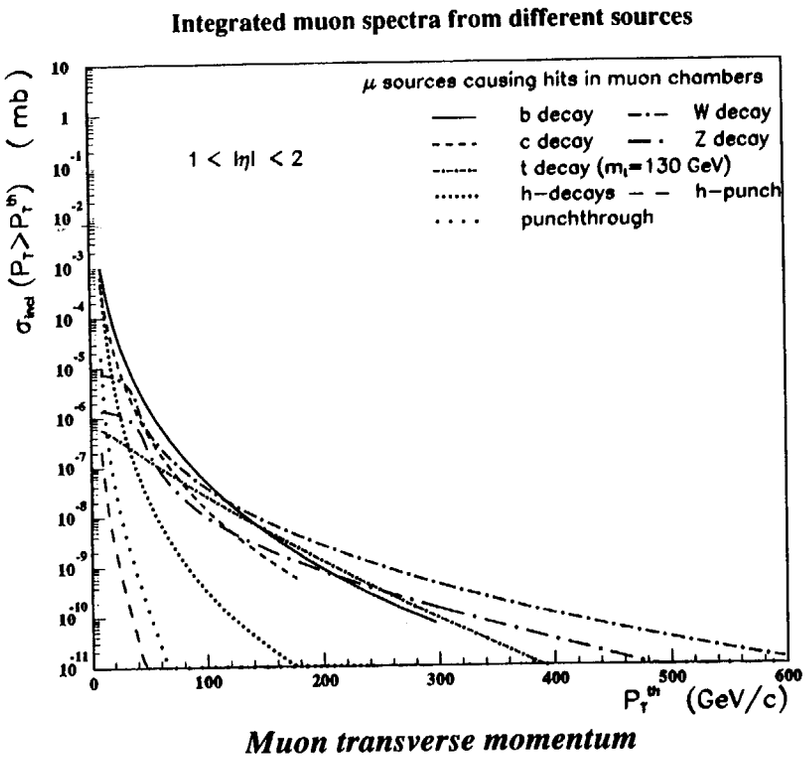

Figure 17: Integral cross sections of various sources of particles in the ATLAS muon system shown as a function of the transverse momentum threshold for $1.0 \leq |\eta| \leq 2.0$.

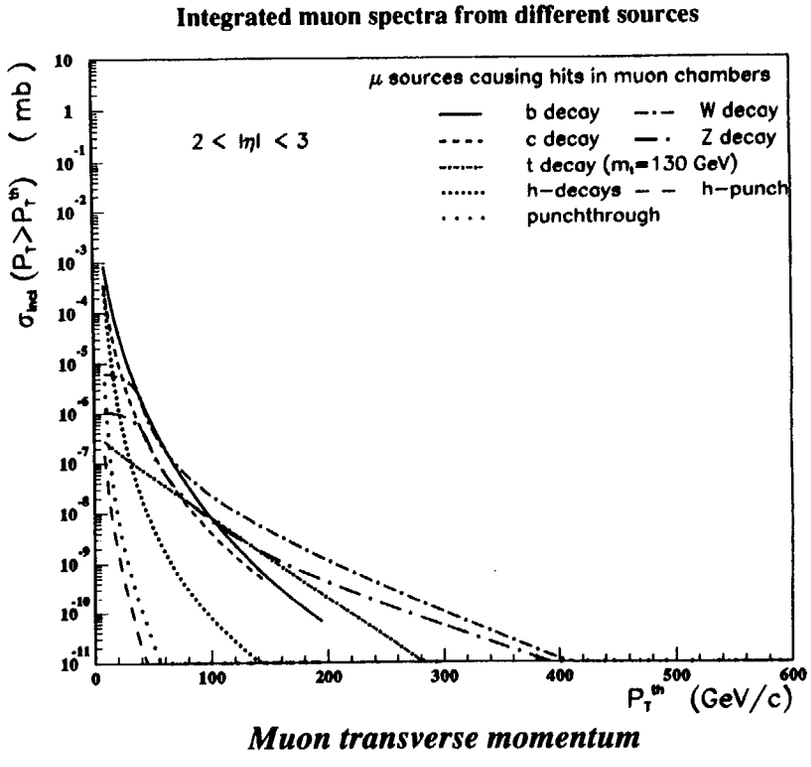

Figure 18: Integral cross sections of various sources of particles in the ATLAS muon system shown as a function of the transverse momentum threshold for $2.0 \leq |\eta| \leq 3.0$.

ATLAS

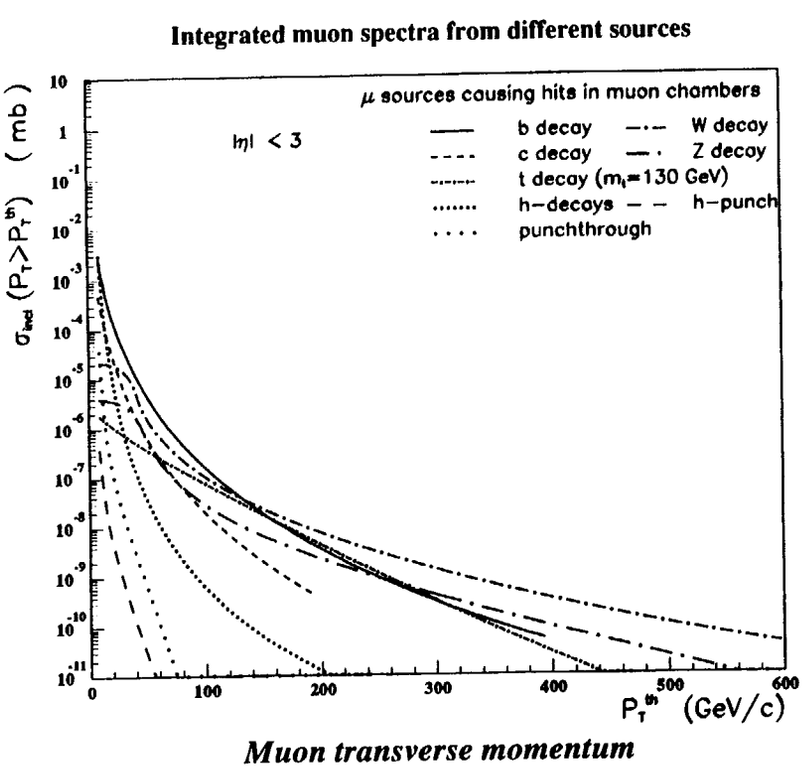

Figure 19: Integral cross sections of various sources of particles in the ATLAS muon system shown as a function of the transverse momentum threshold for $|\eta| \leq 3.0$.

ATLAS

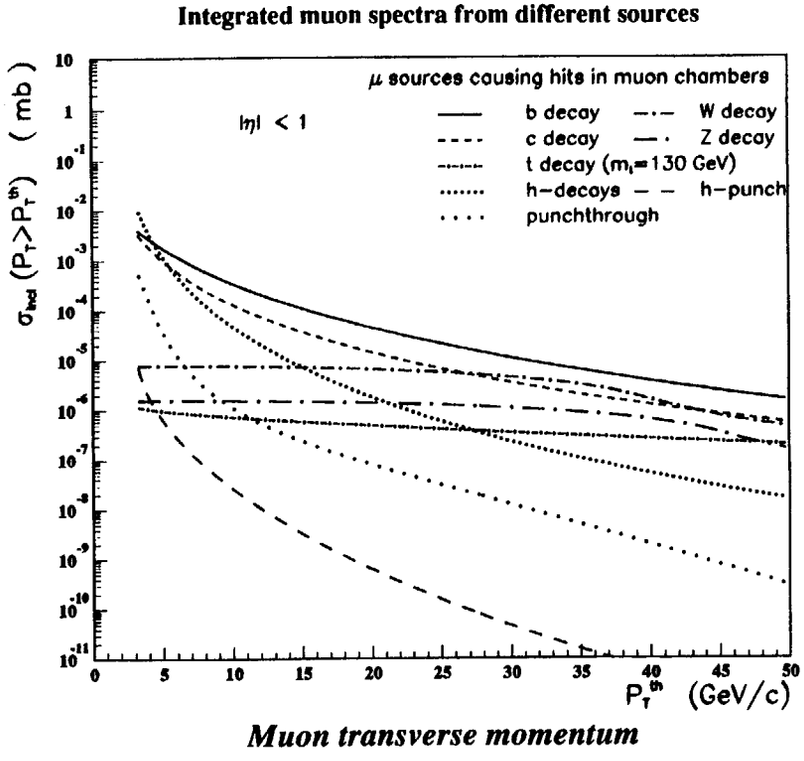

Figure 20: Integral cross sections of various sources of particles in the ATLAS muon system shown as a function of the transverse momentum threshold for $|\eta| \leq 1.0$.

ATLAS

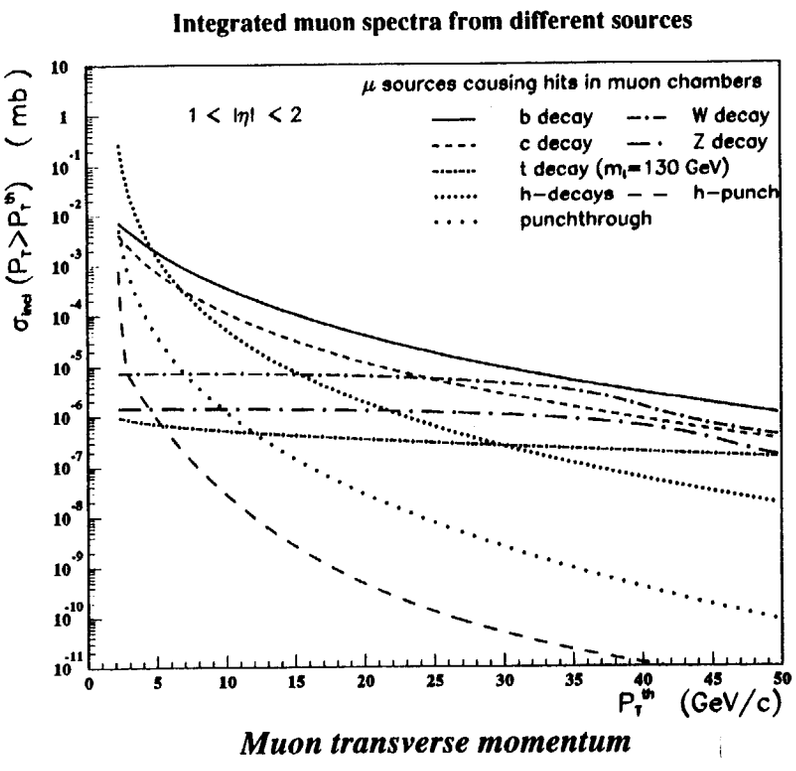

Figure 21: Integral cross sections of various sources of particles in the ATLAS muon system shown as a function of the transverse momentum threshold for $1.0 \leq |\eta| \leq 2.0$.

ATLAS

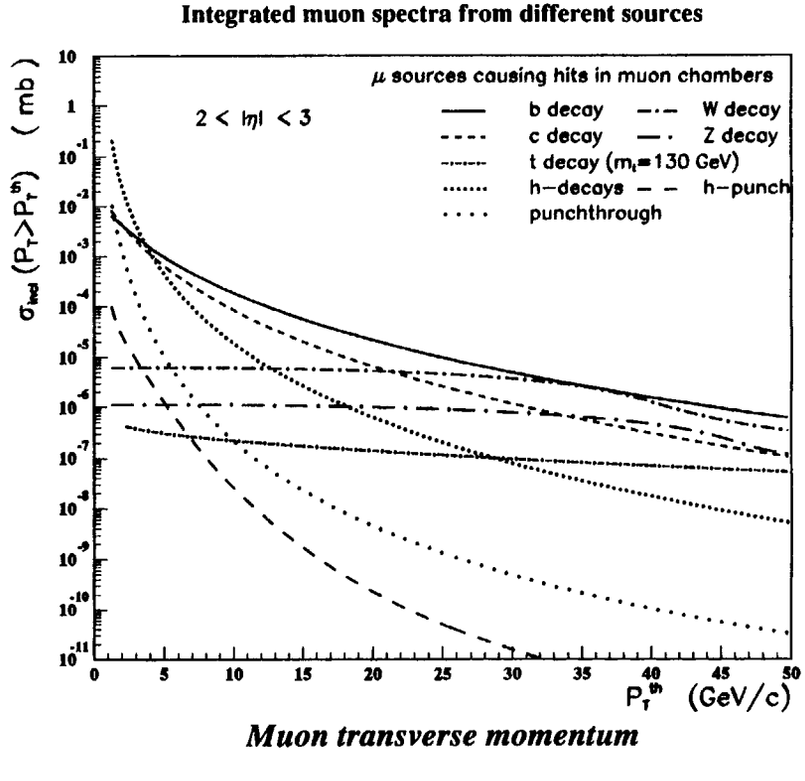

Figure 22: Integral cross sections of various sources of particles in the ATLAS muon system shown as a function of the transverse momentum threshold for $2.0 \leq |\eta| \leq 3.0$.

ATLAS

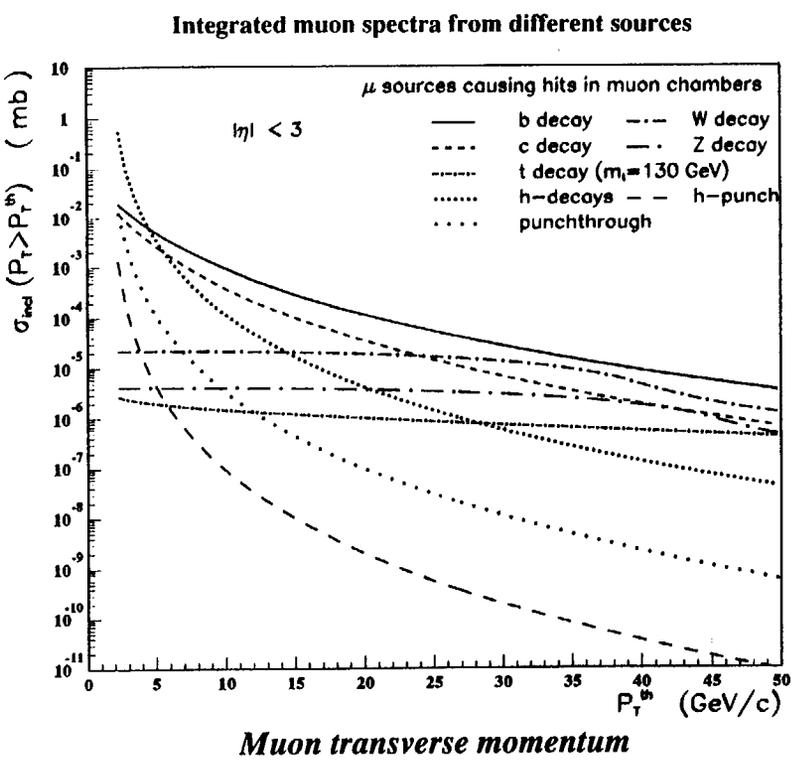

Figure 23: Integral cross sections of various sources of particles in the ATLAS muon system shown as a function of the transverse momentum threshold for $|\eta| \leq 3.0$.

ATLAS

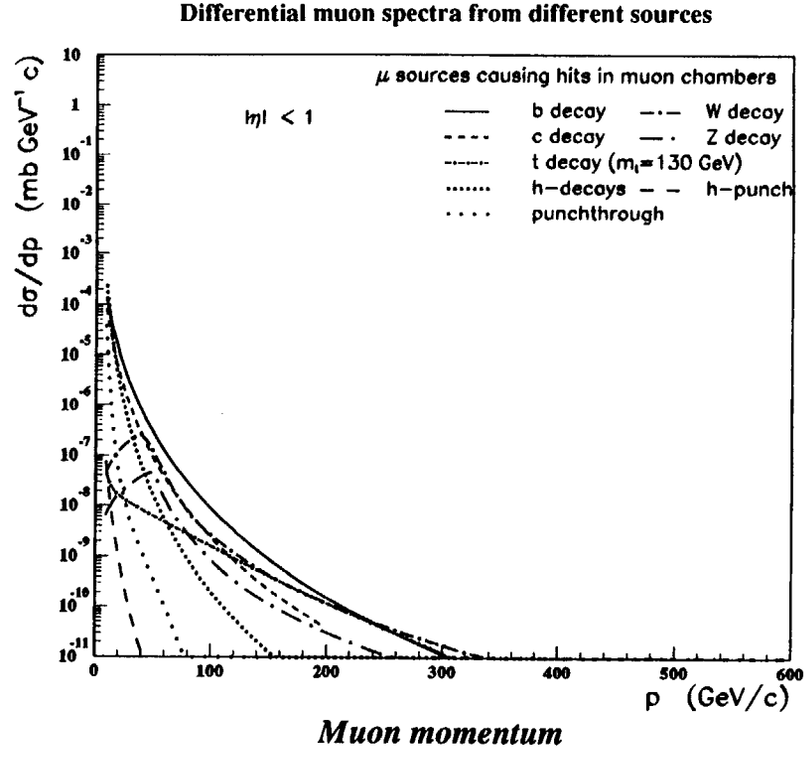

Figure 24: Differential cross sections of various sources of particles in the ATLAS muon system shown as a function of momentum for $|\eta| \leq 1.0$.

ATLAS

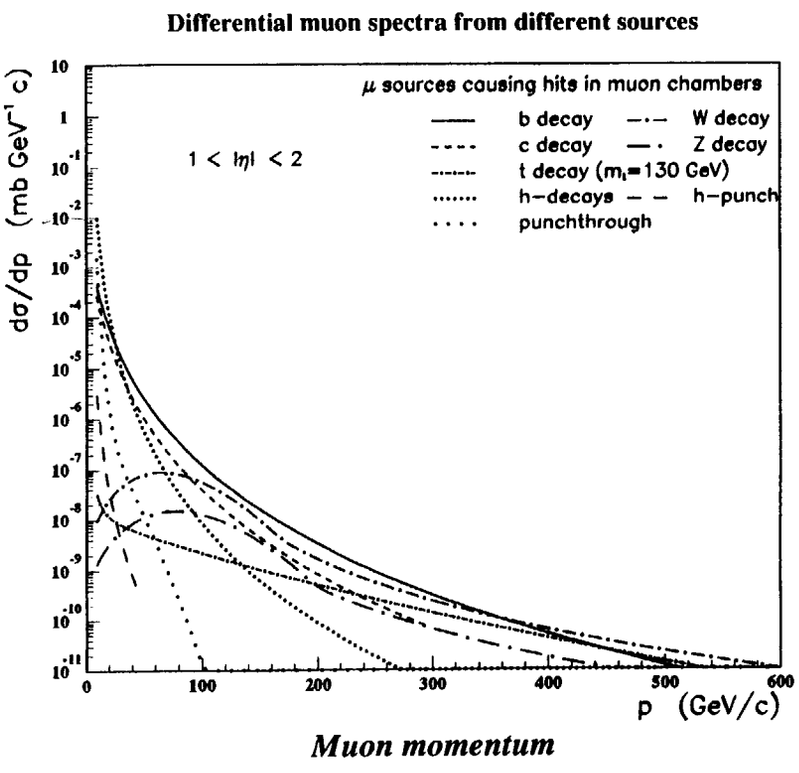

Figure 25: Differential cross sections of various sources of particles in the ATLAS muon system shown as a function of momentum for $1.0 \leq |\eta| \leq 2.0$.

ATLAS

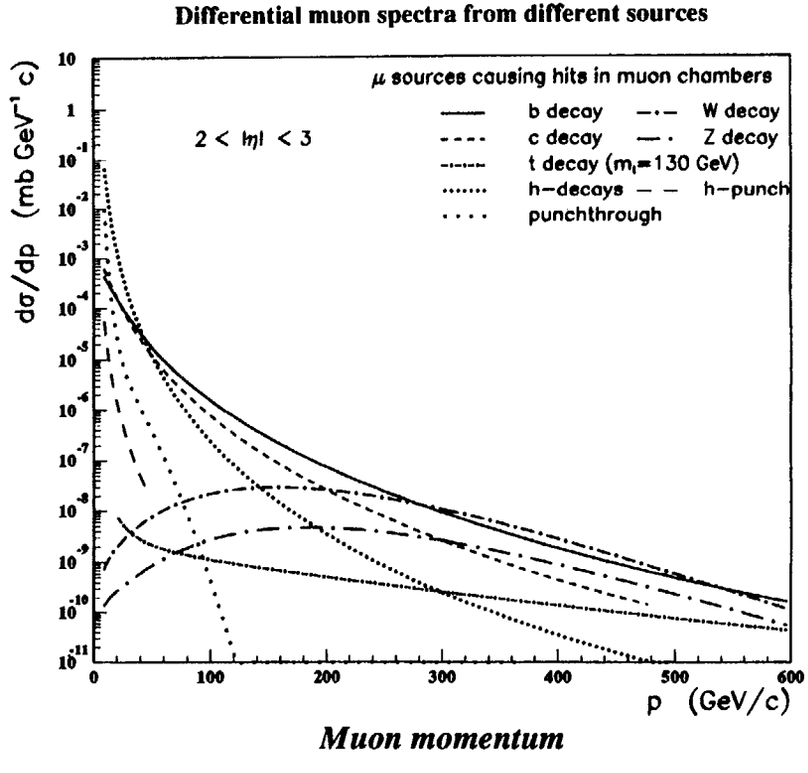

Figure 26: Differential cross sections of various sources of particles in the ATLAS muon system shown as a function of momentum for $2.0 \leq |\eta| \leq 3.0$.

ATLAS

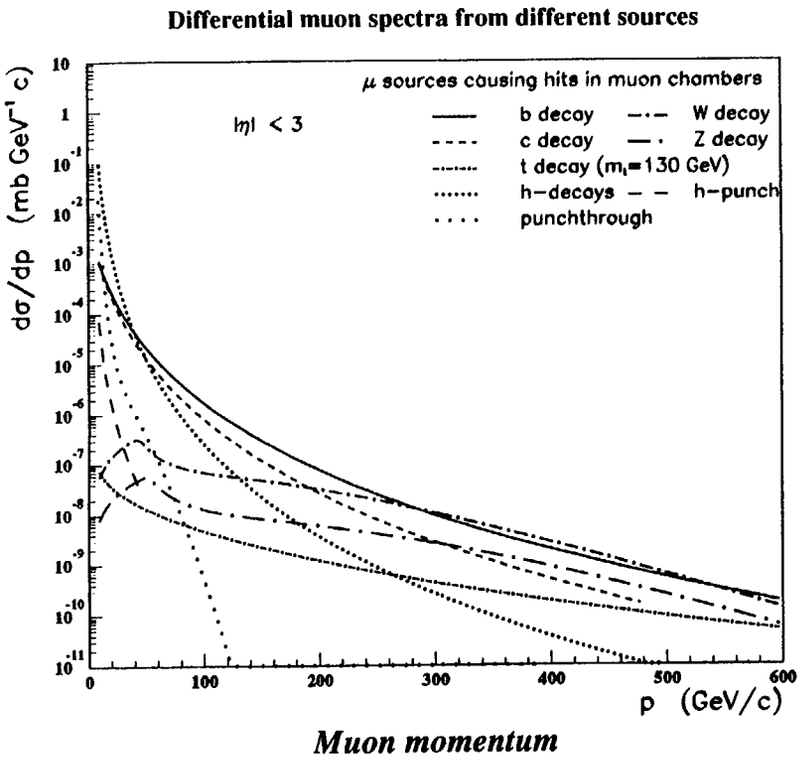

Figure 27: Differential cross sections of various sources of particles in the ATLAS muon system shown as a function of momentum for $|\eta| \leq 3.0$.

ATLAS

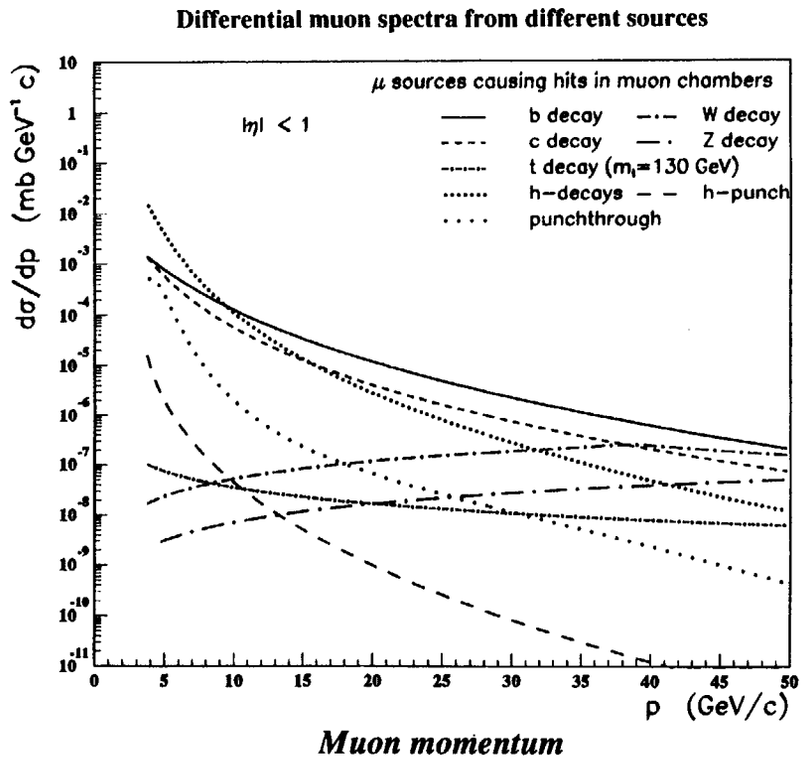

Figure 28: Differential cross sections of various sources of particles in the ATLAS muon system shown as a function of momentum for $|\eta| \leq 1.0$.

ATLAS

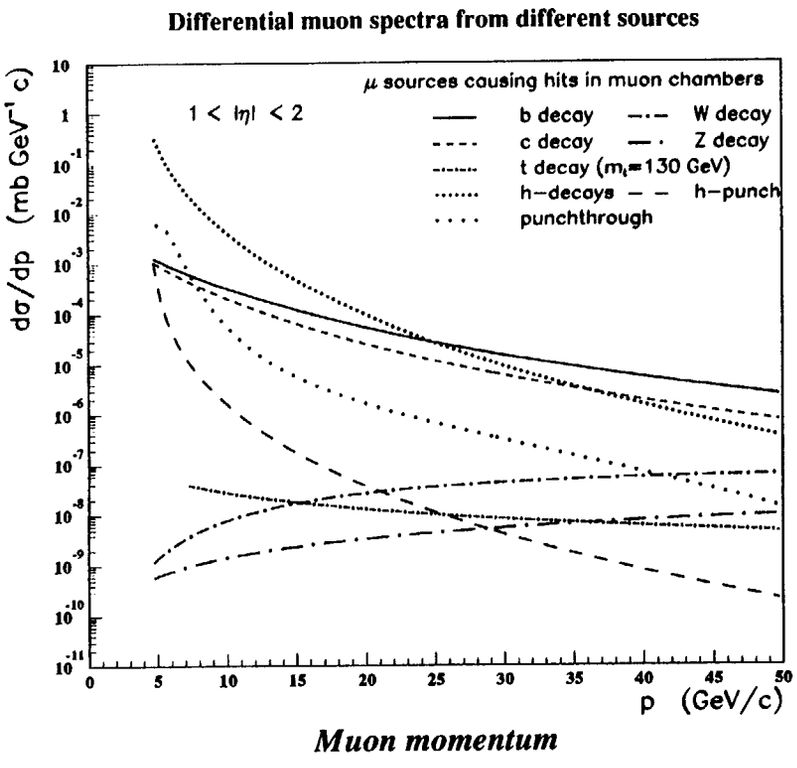

Figure 29: Differential cross sections of various sources of particles in the ATLAS muon system shown as a function of momentum for $1.0 \leq |\eta| \leq 2.0$.

ATLAS

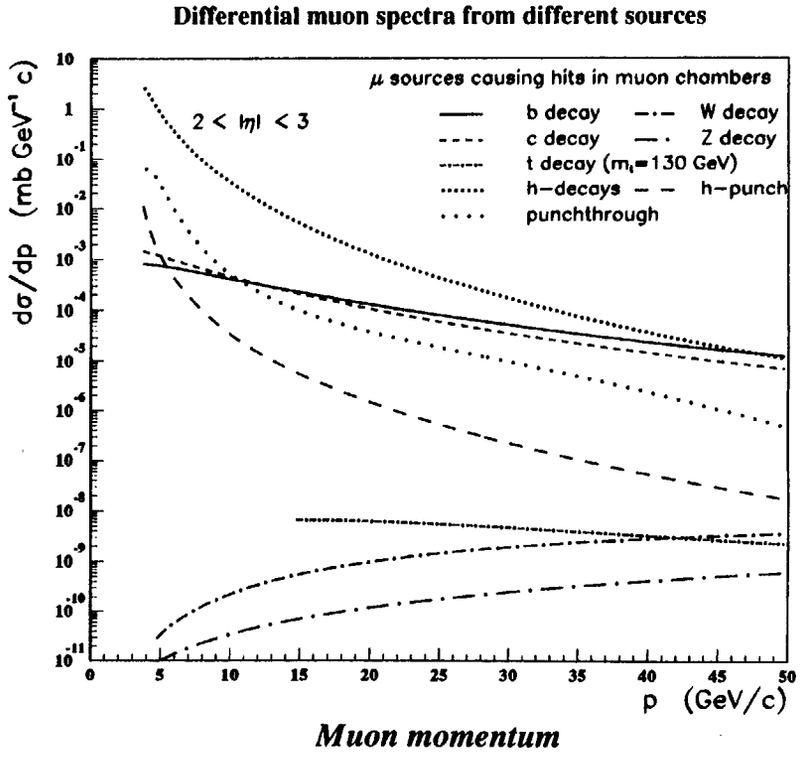

Figure 30: Differential cross sections of various sources of particles in the ATLAS muon system shown as a function of momentum for $2.0 \leq |\eta| \leq 3.0$.

ATLAS

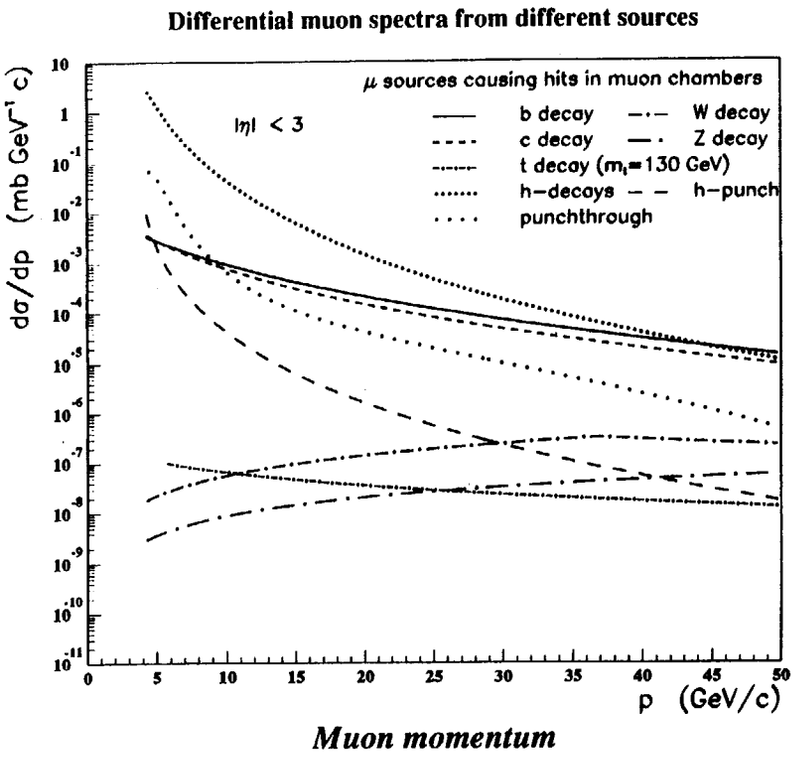

Figure 31: Differential cross sections of various sources of particles in the ATLAS muon system shown as a function of momentum for $|\eta| \leq 3.0$.

ATLAS

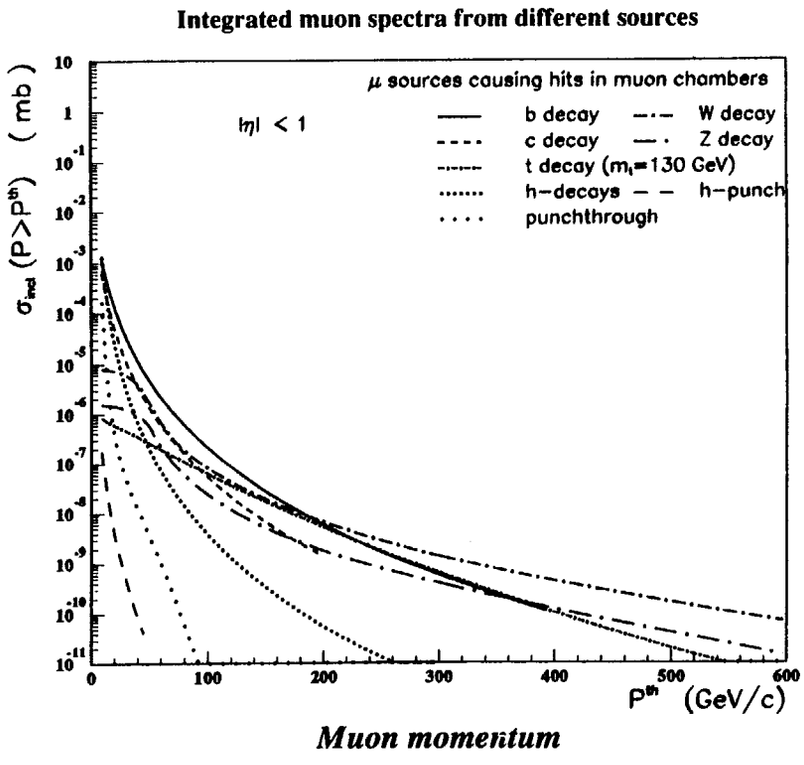

Figure 32: Integral cross sections of various sources of particles in the ATLAS muon system shown as a function of the momentum threshold for $|\eta| \leq 1.0$.

ATLAS

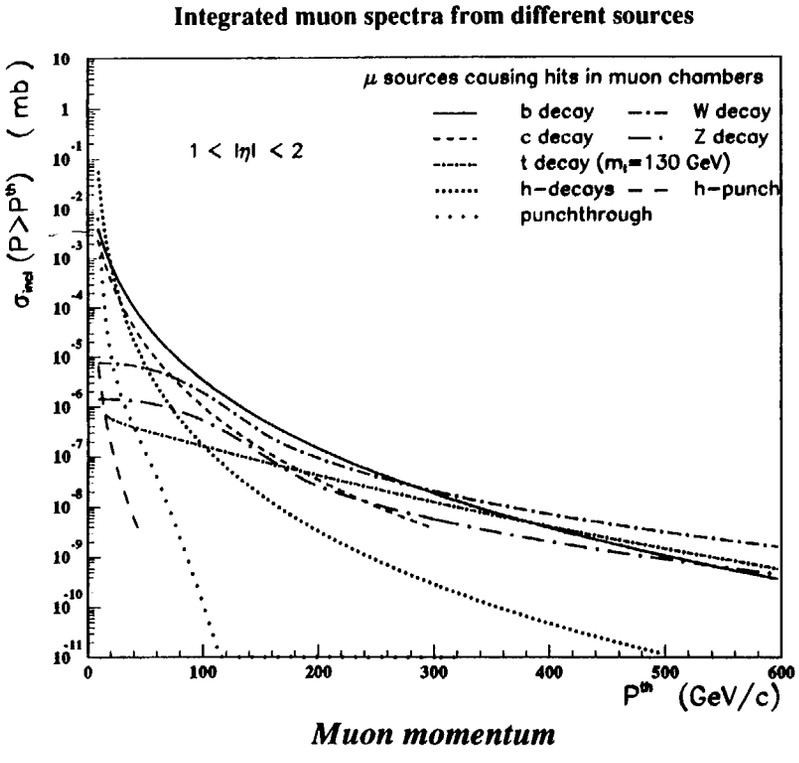

Figure 33: Integral cross sections of various sources of particles in the ATLAS muon system shown as a function of the momentum threshold for $1.0 \leq |\eta| \leq 2.0$.

ATLAS

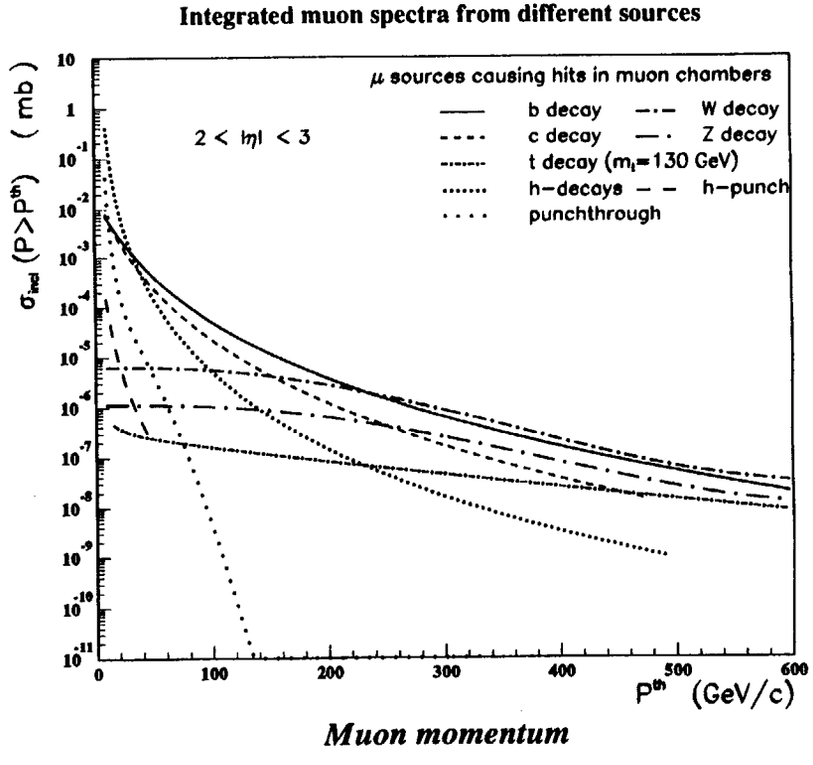

Figure 34: Integral cross sections of various sources of particles in the ATLAS muon system shown as a function of the momentum threshold for $2.0 \leq |\eta| \leq 3.0$.

ATLAS

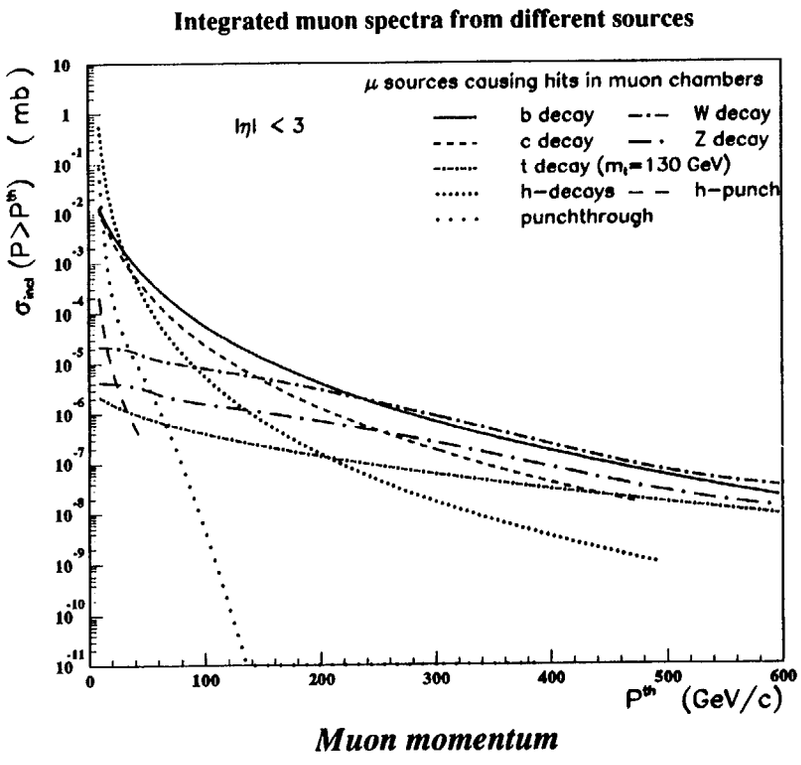

Figure 35: Integral cross sections of various sources of particles in the ATLAS muon system shown as a function of the momentum threshold for $|\eta| \leq 3.0$.

ATLAS

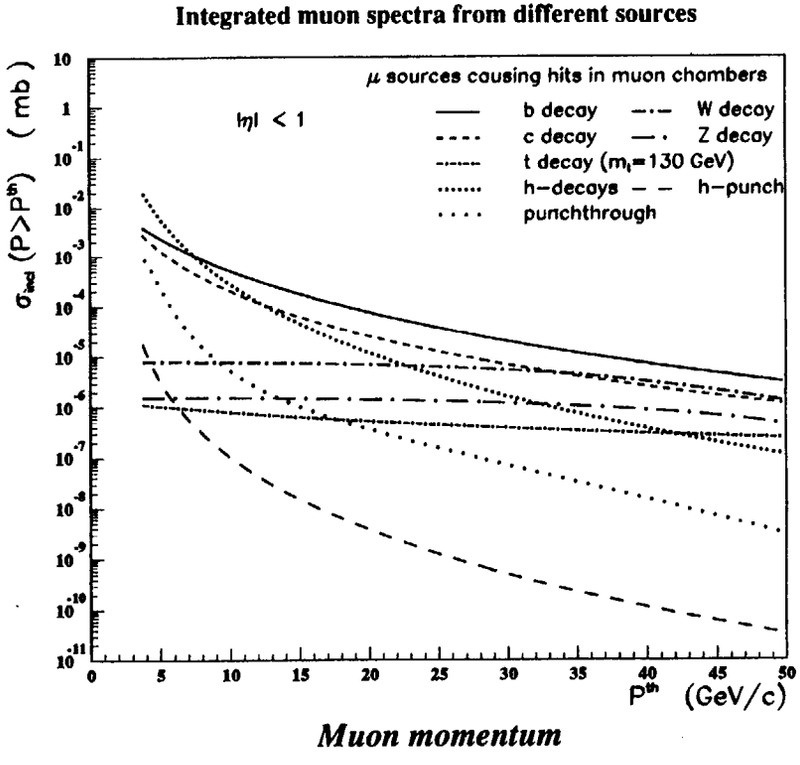

Figure 36: Integral cross sections of various sources of particles in the ATLAS muon system shown as a function of the momentum threshold for $|\eta| \leq 1.0$.

ATLAS

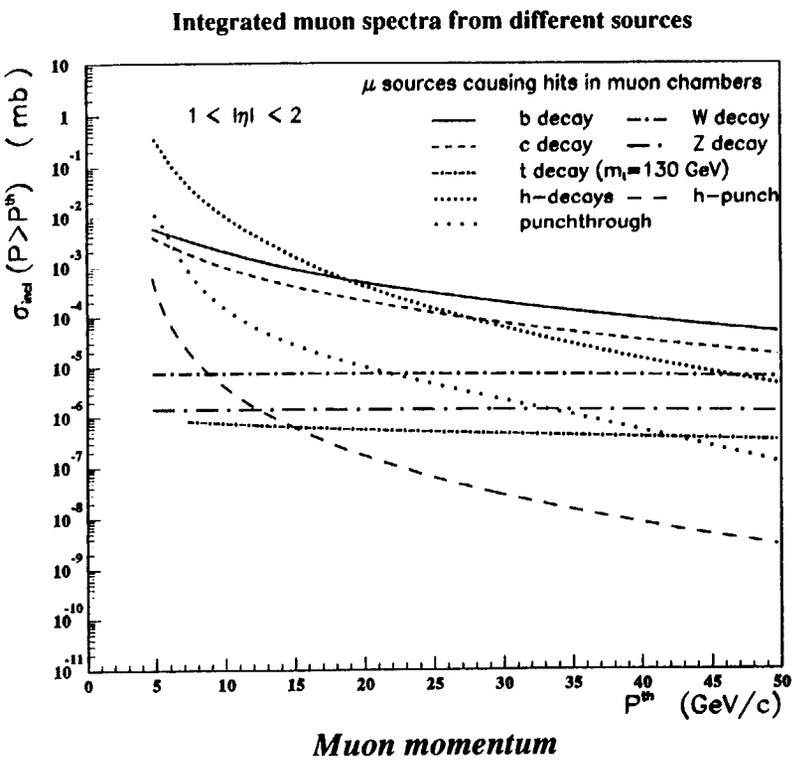

Figure 37: Integral cross sections of various sources of particles in the ATLAS muon system shown as a function of the momentum threshold for $1.0 \leq |\eta| \leq 2.0$.

ATLAS

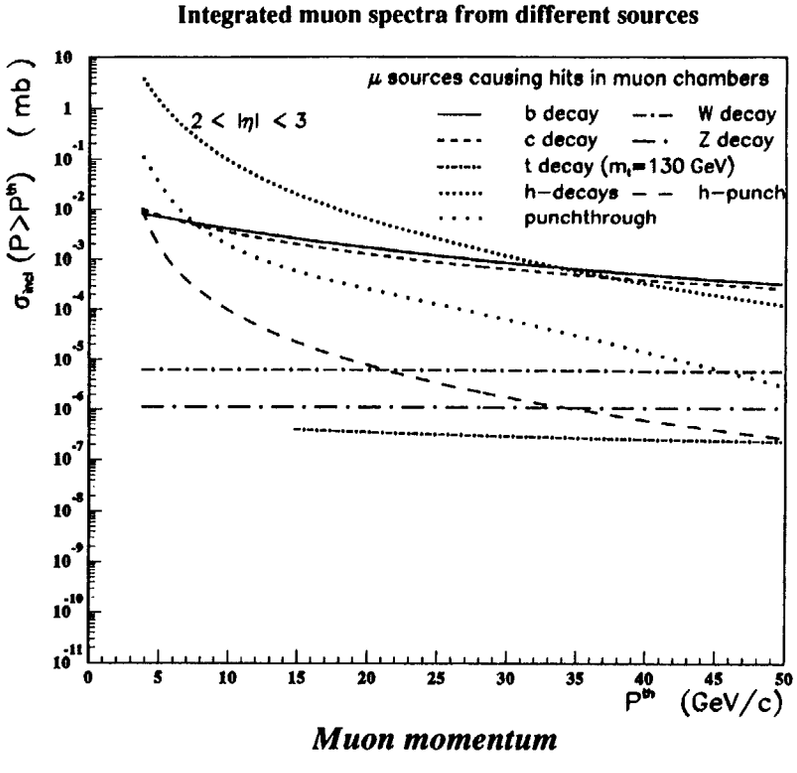

Figure 38: Integral cross sections of various sources of particles in the ATLAS muon system shown as a function of the momentum threshold for $2.0 \leq |\eta| \leq 3.0$.

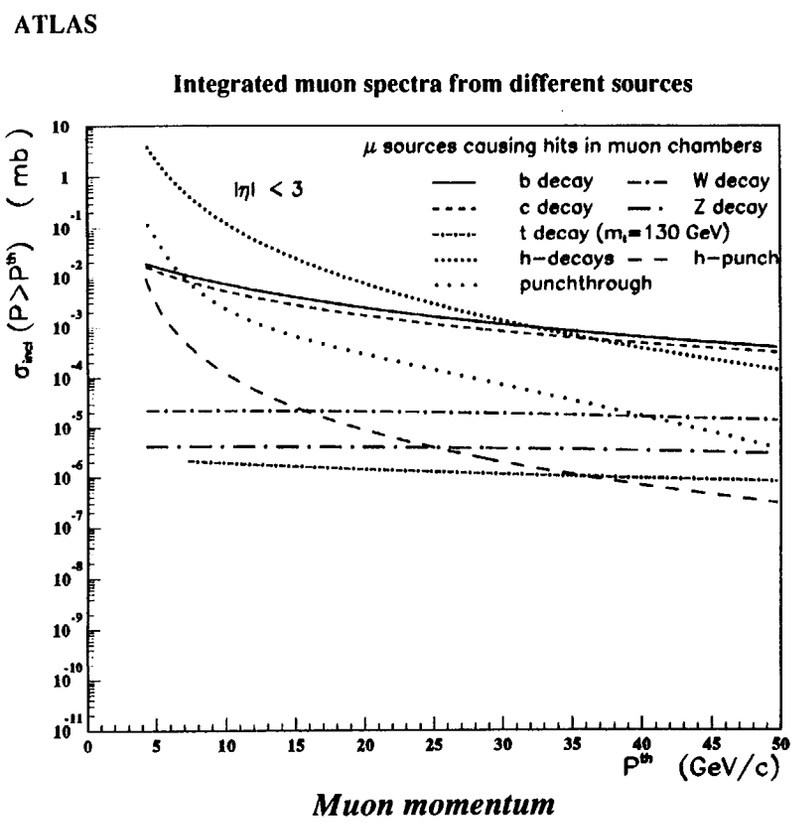

Figure 39: Integral cross sections of various sources of particles in the ATLAS muon system shown as a function of the momentum threshold for $|\eta| \leq 3.0$.

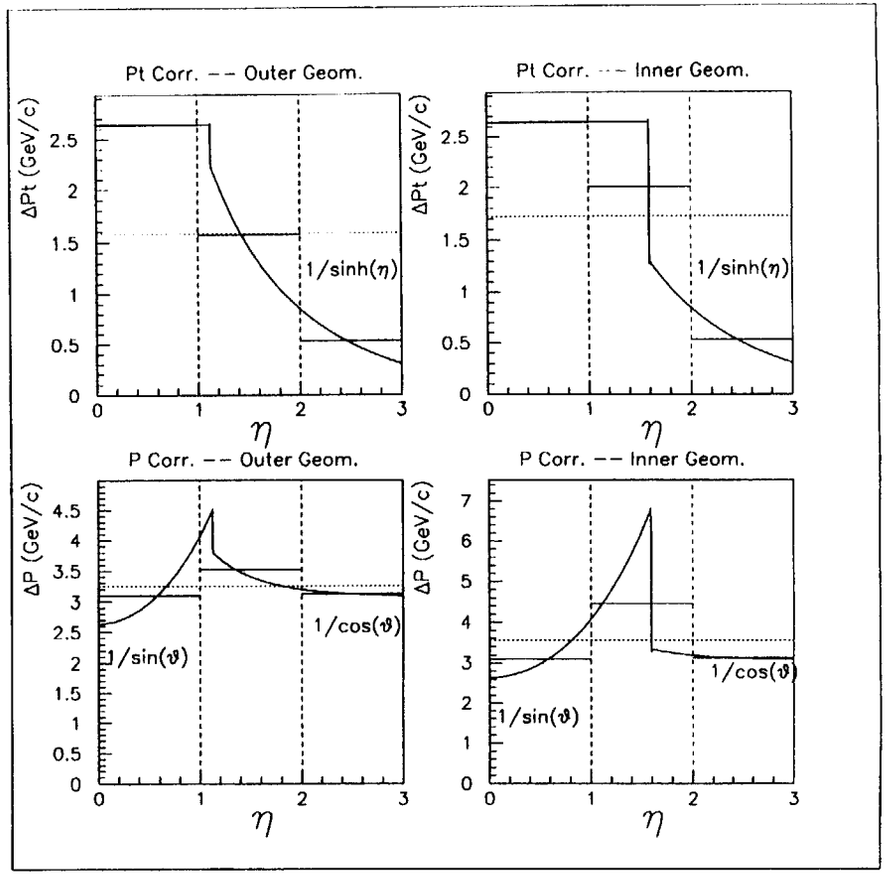

Figure 40: Shift in the momentum and transverse momentum of a particle shown as a function of pseudorapidity. Here inner and outer refer to the inner cavity and outer cavity geometry and their implications on the angle at which the transition from barrel to endcap occurs. The vertical lines indicate the regions over which the functions are integrated and the horizontal lines indicate the average values of the functions over these ranges.